



---

## Detector coincidence system with scintillators and calibration of the AN2000 accelerator

Chiara Baron - 2027581 - chiara.baron1@studenti.unipd.it

Emma Reniero - 2056750 - emma.reniero@studenti.unipd.it

Anna Vigolo - 2028849 - anna.vigolo.1@studenti.unipd.it

March 2022 - January 2023

This experimental activity is divided into two parts.

The first one is devoted to the characterization of two LaBr<sub>3</sub>(Ce) and two CeBr<sub>3</sub> scintillator detectors using different radioactive sources. We calculated the efficiency of the detectors as a function of the distance and of the energy; eventually we tested the time response of the detectors performing a measurement of the speed of light.

The second part is the energy calibration of the AN2000 accelerator (Laboratori Nazionali di Legnaro) using two resonant reactions produced with a beam of protons on an Aluminium target.

---

**CONTENTS**

<b>I.</b> Introduction	1
<b>1.</b> Scintillation Detectors	1
<b>2.</b> Germanium Detectors	2
<b>3.</b> Digitizer	3
<b>A.</b> DPP-PHA mode	3
<b>B.</b> PSD mode	5
<b>4.</b> Sources	6
<b>II.</b> I part: Characterization of the scintillation detectors	7
<b>1.</b> Experimental set up	7
<b>2.</b> Adopted notation on the errors	7
<b>3.</b> Energy calibration	8
<b>4.</b> Width calibration	9
<b>5.</b> Intrinsic activity of the LaBr <sub>3</sub> (Ce) detectors	12
<b>6.</b> Background evaluation:	13
<b>7.</b> Signal to noise ratio	15
<b>8.</b> Study of the coincidences	18
<b>9.</b> Efficiency	21
<b>A.</b> Efficiency with integral under the peaks	21
<b>B.</b> Efficiency from Na coincidences	24
<b>C.</b> Efficiency from Co coincidences	24
<b>10.</b> Efficiency vs distance and Efficiency vs energy	26
<b>11.</b> Speed of light	28
<b>III.</b> II part: calibration of the AN2000 accelerator	31
<b>1.</b> Experimental set up	31
<b>2.</b> Resonant reactions and Yield	32
<b>3.</b> Data acquisition	33
<b>4.</b> Adopted notation on the errors	34
<b>5.</b> Data analysis	35
<b>A.</b> Energy calibration of the detectors	35
<b>B.</b> Background subtraction for LaBr <sub>3</sub> (Ce) detector	36
<b>C.</b> Background subtraction for Germanium detector	36
<b>D.</b> Resonances at 992 keV with LaBr <sub>3</sub> (Ce) detector, data collected on November 23, 24 and 25, 2022	37
<b>E.</b> Resonances at 1664 and 1684 keV with LaBr <sub>3</sub> (Ce) and Germanium detectors, data collected on November 24 and 25, 2022	38
<b>F.</b> Fitting of data with an arctangent function	40
<b>IV.</b> Conclusions	45
References	45

## I. INTRODUCTION

In the laboratory we used two different types of scintillator detectors ( $\text{LaBr}_3(\text{Ce})$  and  $\text{CeBr}_3$ ) and a germanium detector. In this introductory part we summarise the main characteristics of these detectors and describe the digital acquisition system used to process the acquired signals. Then we give details on the radioactive sources we used for calibrating and characterizing the detectors.

Since the experiment is divided into two different parts, one devoted to the characterization of the scintillators and one to the calibration of the AN2000 accelerator, the report is divided into two main sections. In each section we give a description of the adopted experimental set up and we report the data analysis. Eventually, the obtained results are collected in the conclusions.

### 1. Scintillation Detectors

One of the goals of this experiment is the characterization of four inorganic scintillation detectors and the description of their response to gamma radiation. In this type of detectors, the incoming radiation produces primary electrons when interacting with the crystal; these primary electrons lose their energy creating secondary electron-hole pairs. Since the inorganic crystals are electrical insulators, the valence and the conduction bands are separated by a large gap. If the incident gamma gives to a valence electron enough energy, the latter is able to pass to the conduction band; then the electron de-excites emitting an high energy gamma. However this process is not efficient for detection: often the emitted photon is not in the visible range and so it is difficult to detect. A possible solution to this problem is the introduction of impurities (called activators) inside the crystal: such a process allows to modify the band structure of the crystal, creating new energy states in the forbidden gap. These states can be populated by the excited electron and the photon emitted during the de-excitation process is usually emitted in the visible range. The band gap structure of a doped scintillator is displayed in Figure 1 [1].

The electric signal is generated by the conversion of photons coming from the de-excitation process into electrons, which are collected. At this stage usually an amplifier is needed: most commonly the scintillator crystal is coupled to a photomultiplier tube. Then the amplified signal is sent to the digitizer

In this experiment two types of inorganic crystals were used: two  $\text{LaBr}_3(\text{Ce})$  and two  $\text{CeBr}_3$ .

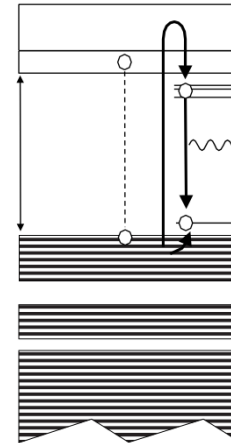


Figure 1 Scheme of the band structure in scintillators. Picture taken from [1].

- **$\text{LaBr}_3(\text{Ce})$ :** This inorganic crystal is characterized by a high effective Z, high density and fast decay times. In addition, its energy resolution is extremely high compared to other scintillator crystals, as it is possible to see in Figure 2 [2]. The downsides are mainly connected to the high intrinsic activity; a detailed description of the intrinsic activity is given in Subsection II.5. The two  $\text{LaBr}_3(\text{Ce})$  detectors used in this experiment have a 10 cm diameter scintillator crystal, coupled to photomultiplier tube.
- **$\text{CeBr}_3$ :** This inorganic crystal is used for its excellent timing characteristics. In fact, it has both a short rise time and a fast decay time. What is more, the light yield is rather high [2]. As part of this work, its timing resolution was tested measuring the speed of light. The two  $\text{CeBr}_3$  used in this experiment have a  $51 \text{ mm}^2$  diameter scintillator crystal, coupled to Hamamatsu R6231 PMT tube magnetically shielded.

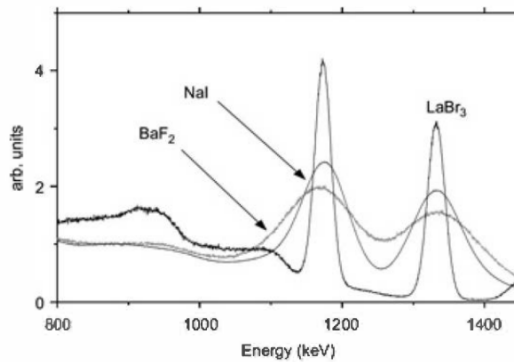


Figure 2 Comparison of the  $^{60}\text{Co}$  spectrum measured with 1-inch x 1-inch  $\text{LaBr}_3$ ,  $\text{NaI}$  and  $\text{BaF}_2$ . Picture taken from [2].

## 2. Germanium Detectors

In the calibration of the AN2000 accelerator we used a Germanium detector to acquire the signal of the gamma rays produced in the reactions. Germanium is a semiconductor and the properties of these kind of materials are exploited to extract the signals. In the case of semiconductors, when we are in presence of a collection of atoms, the electrons are disposed into a band structure. The highest occupied band is called valence band and between this band and the higher conduction band there is an energy gap of the order of 1 eV. Since the band gap is so small, the energy necessary to promote an electron from the valence to the conduction band is small and comparable to the energy given by thermal excitation. For this reason, cooling the material is crucial to reduce the noise. The interaction of gamma rays with the semiconductor material gives the electrons enough energy to be promoted to the conduction band; often also electrons in lower bands are excited and when they are promoted they leave a hole. When such a process takes place, a rearrangement mechanism takes place: holes and electrons migrate in order to achieve a configuration in which the excited electrons are placed at the bottom of the conduction band, while the holes migrate to the top of the valence band. During the rearrangement process, further excitation may happen and if an electric field is applied, the charge carriers can be collected. Figure 3 shows the typical band structure of a semiconductor compared to that of an insulator and a conductor; in addition, the rearrangement mechanism of electrons and holes is depicted.

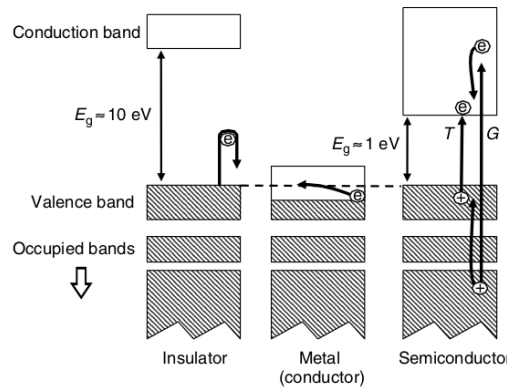
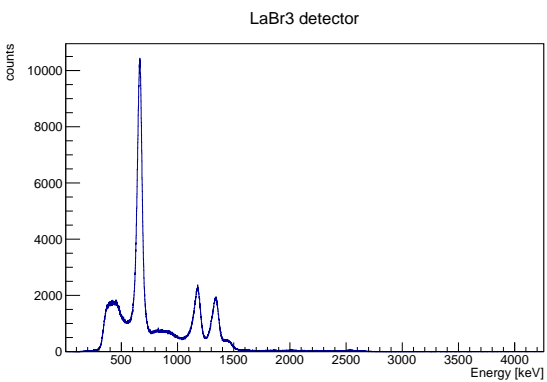
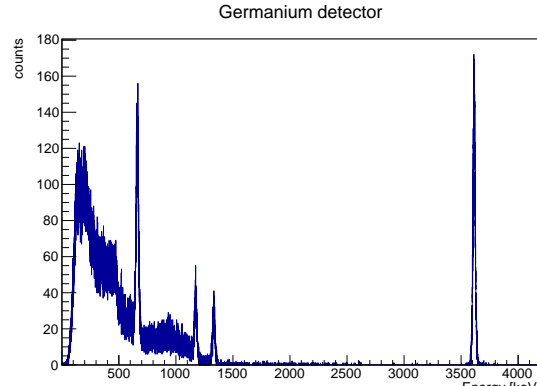


Figure 3 Scheme of the band structure in a semiconductor compared to an insulator and a conductor. Picture taken from [1].

Germanium is widely used because it has a rather high atomic number (32) and so its absorption coefficient is high enough to ensure the complete absorption of gamma rays of higher energy compared to other semiconductors, such as Silicon. In addition, it is possible to produce pure germanium crystals, since impurities and defects may alter the charge collection, for example becoming traps for holes and electrons [1]. The major downside of using a germanium detector is that it must be cooled down. For this reason, in our experimental set up, the Germanium is connected to a dewar containing liquid nitrogen. The main advantage of using a semiconductor detector instead of a scintillation

detector is in the increased energy resolution. As a comparison, Figures 4a and 4b show a spectrum acquired with a LaBr<sub>3</sub>(Ce) scintillator and a spectrum acquired simultaneously with a germanium detector. In both cases the sources are the same; the different statistics are due to the different distance from the source.

(a) Spectrum acquired with a LaBr<sub>3</sub>(Ce) detector

(b) Spectrum acquired with a Germanium detector

Figure 4 4a shows a spectrum acquired with a LaBr<sub>3</sub>(Ce) detector, while 4b shows a spectrum acquired with a Germanium detector. The peak at about 3600 keV present in the Germanium detector and absent in the LaBr<sub>3</sub>(Ce) detector is due to the pulser.

### 3. Digitizer

In the experiment we used a V1730 CAEN board to acquire and digitize the signal coming from the detectors; the board was coupled to the CAEN CoMPASS software. The usage of this type of digitizer allowed us to avoid the traditional analog chain used for radiation spectroscopy. The signal coming from the pre-amplifier was sent directly to the board and the software allowed to set different parameters optimizing the acquisition. In the following two subsection we report the details on the acquisition software. To write this part we used as references the CAEN manuals [3], [4], [5].

#### A. DPP-PHA mode

The Digitizer runs a DPP-PHA firmware (see Fig. 5 for the scheme) that works as a Digital Multi Channel Analyzer. This system can be managed and the parameters can be changed depending on the kind of radiation and detectors thanks to the CAEN CoMPASS software that also allows to perform the data readout.

As one can see in Fig. 5 the DPP-PHA directs the signal into two units: the Trigger and Timing Filter, which identify the pulses and calculate the time at which an event is generated (allowing to reduce the noise and prevents to trigger the false events) and the Energy Filter (Trapezoidal). The final output of CoMPASS is an energy spectrum where the counts depends on the channels.

The **trapezoidal filter** can be briefly described as a filter able to transform the typical long-tailed exponential signal generated by a Charge Sensitive Preamplifier into a trapezoid whose height is proportional to the amplitude of the input pulse that is to the energy released by the particle in the detector (see Fig. 6). It is important to highlight that this trapezoid filter plays more or less the same role of the Shaping Amplifier in a traditional analog acquisition system.

The main parameters for the trapezoid are: the **baseline**, the **rise time** (which is the time needed for the signal to reach its maximum value and has the same role of the shaping time in the shaping amplifier), the **flat top** (width of the minor basis of the trapezoid) and the **peaking time** (the time needed to reach the middle point of the flat top).

The energy filter includes a baseline restorer that operates on the trapezoidal filter output and calculates the baseline by averaging a programmable number of points before the start of the trapezoid. The baseline is then frozen for the trapeze duration and used for the height calculation. Once the trapezoid is returned to the baseline, the averaging

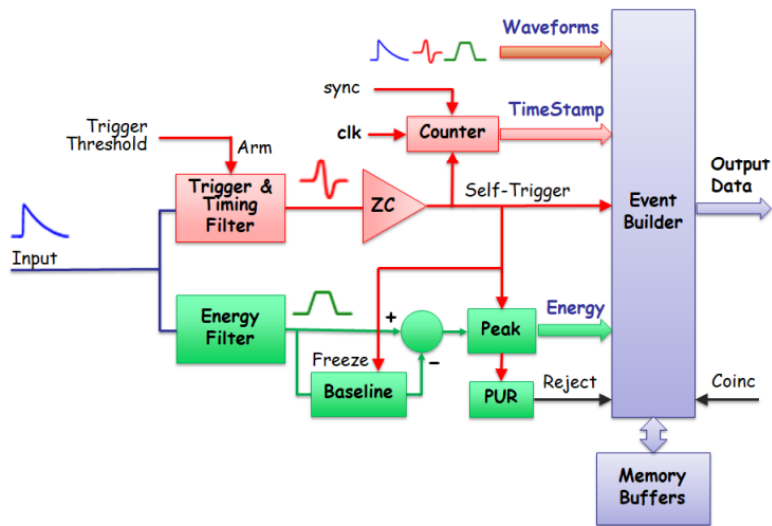


Figure 5 Scheme of the DPP-PHA firmware

restarts to run.

The trapezoid requires an accurate **pole-zero adjustment** to guarantee the correct return to the baseline at the end of the falling edge. To correctly set the pole-zero the user must take care of setting the proper trapezoidal pole zero value (which corresponds also to the input decay time) to avoid either undershoot or overshoot effects.

If two events are separated by less than the trapezoid duration, then the relevant trapezoids overlap (**pile up**). The trapezoid duration is defined as the sum of the trapezoid rising time, the flat top and the peak holdoff, which starts at the end of the Flat Top. The peak holdoff is used to store heights of only well-separated pulses, ensuring a precise baseline calculation for each trapezoid. Piled up events are also saved in the memory but they do not fill the energy histogram; furthermore, the energy spectrum can be corrected run-time by a statistical redistribution of the missed energies over the spectrum acquired within a specific time slot.

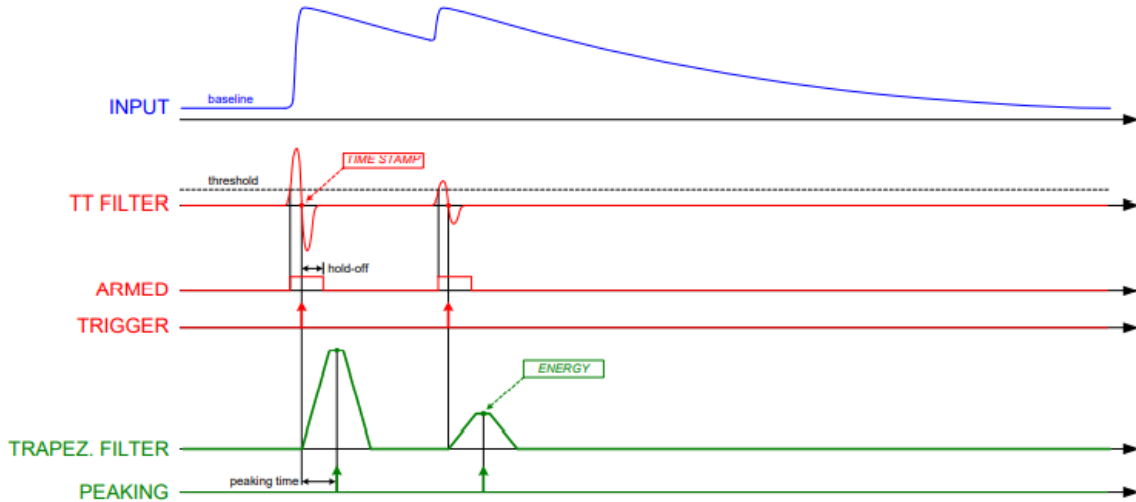


Figure 6 Scheme of the Trigger and Timing filter plus the Energy Filter

## B. PSD mode

In order to have a better time resolution for the speed of light measurement it is necessary to use the DPP-PSD firmware that integrates the charge that arrives from the detectors and calculates the PSD (Pulse Shape Discriminator) factor which is the ratio between the tail of the input signal ( $Q_L - Q_S$ ) and the total charge  $Q_L$ .

The main functionalities of a digitizer running DPP-PSD firmware are:

- Selection of the events with a digital leading edge discrimination or a digital constant fraction discrimination;
- Input signal baseline (pedestal) calculation and pedestal subtraction for energy calculation;
- Single gate integration for the energy spectra calculation;
- Double integration of the prompt and delayed charge for Pulse Shape Discrimination.

Once an event is selected, the signal is delayed by a programmable number of samples (corresponding to the “pre-trigger” value) to be able to integrate the pulse before the trigger (“Pre- Gate”). The gates for charge integration are then generated and received by the charge accumulator before the signal. While the gates are active, the baseline remains frozen until the last averaged value and its value is used as charge integration reference. For the whole duration of a programmable “trigger hold-off” value, other trigger signals are inhibited.

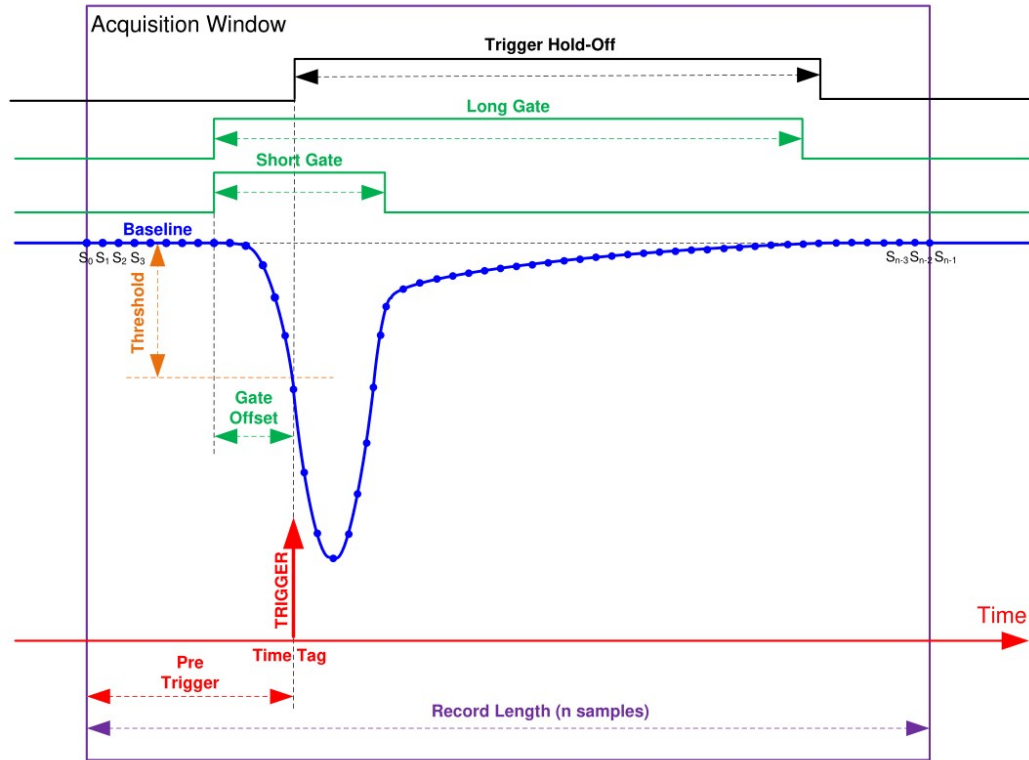


Figure 7 Diagram summarizing the DPP-PSD parameters.

#### 4. Sources

We used three types of radioactive sources:  $^{22}\text{Na}$ ,  $^{60}\text{Co}$  and  $^{137}\text{Cs}$ . The nucleus of  $^{22}\text{Na}$  decays with a branching ratio of 90.4 %  $\beta^+$  to the  $2^+$  excited state of  $^{22}\text{Ne}$ , which settles to ground state emitting a  $\gamma$ -ray of  $(1274.537 \pm 0.007)$  keV<sup>1</sup>. In the 9.6 % of the cases  $^{22}\text{Na}$  decays by electron capture to the same  $^{22}\text{Ne}$  level. When the positron originated from the  $\beta^+$  decay encounters an electron in the medium, it forms an unstable bound state called positronium, whose preferred decay mode is the annihilation into 2  $\gamma$ -rays both with 511 keV energy. Due to momentum conservation, these two  $\gamma$  are emitted in a back to back fashion.

The  $^{60}\text{Co}$  nucleus decays  $\beta^-$  with a branching ratio of 99.88 % to the  $4^+$  excited state of  $^{60}\text{Ni}$ , which emits at first a  $\gamma$  ray of  $(1173.228 \pm 0.003)$  keV to reach a lower  $2^+$  excited level, and then settles to ground state emitting a  $\gamma$  of  $(1332.501 \pm 0.005)$  keV. In the 0.12 % of the cases the  $^{60}\text{Co}$  decays  $\beta^-$  to the  $2^+$  level which then settles to the ground state emitting a  $\gamma$  of 1333 keV.

The  $^{137}\text{Cs}$  nucleus decays  $\beta^-$  with a branching ratio of 94.6 % to the  $11/2^-$  excited state of  $^{137}\text{Ba}$ , which settles to ground state emitting a  $(661.657 \pm 0.003)$  keV gamma ray. In the remaining 5.4 % cases,  $^{137}\text{Cs}$  decays directly to the ground state of  $^{137}\text{Ba}$ . Figure 8 shows the decay schemes of these nuclei.

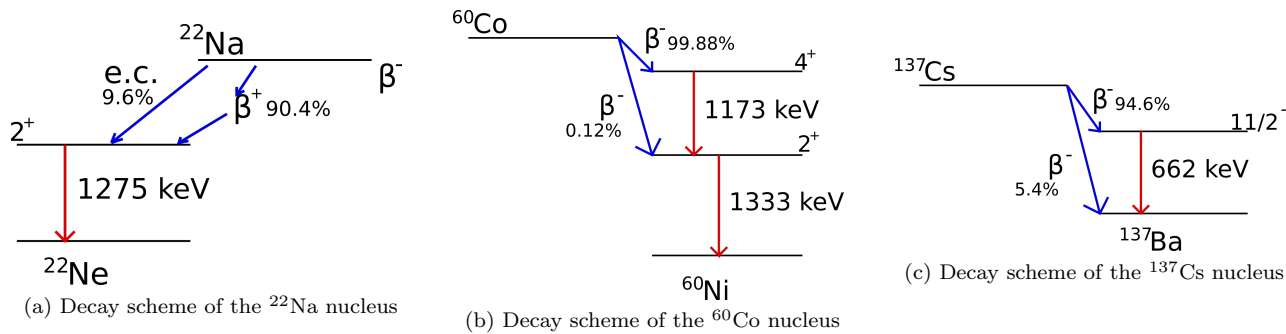


Figure 8 Decay schemes of the radioactive source used during the experiment.

<sup>1</sup> The energies of the gamma rays are taken from <https://www.nndc.bnl.gov/nudat3/>

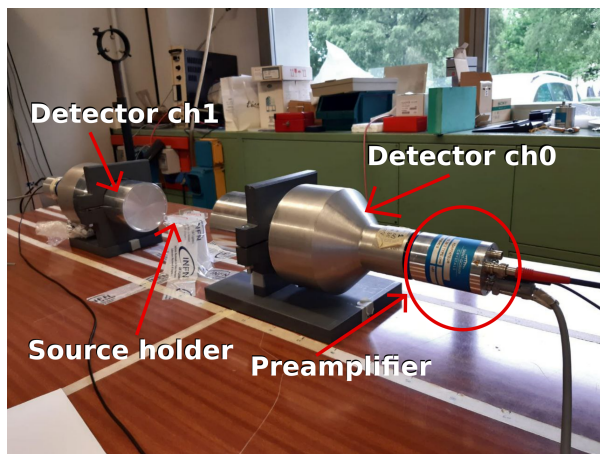
## II. I PART: CHARACTERIZATION OF THE SCINTILLATION DETECTORS

### 1. Experimental set up

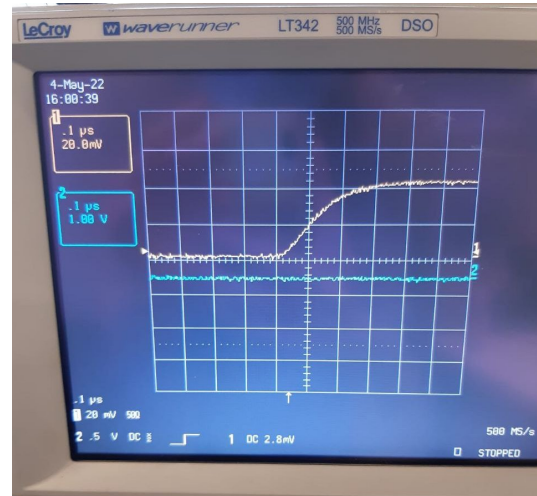
In the first part of the experiment, the experimental set up comprised:

- Two kinds of cylindrical scintillators ( $\text{LaBr}_3(\text{Ce})$ ) and  $\text{CeBr}_3$ , coupled to photomultiplier tubes.
- Digitizer: V1730 CAEN board.
- Different types of connectors and cables; in particular two lemo cables: the shorter one connected to ch0 of the digitizer; the longest to ch1.
- An oscilloscope used to visualize directly the signals coming from the detector.

The detectors, as Figure 9a shows, were mounted on a table and we placed the source holder between them. The  $\text{LaBr}_3(\text{Ce})$  detectors had specific holders, while the  $\text{CeBr}_3$  detectors were placed directly on the table. The sources were placed in such a way to be at half the height of the sensible region of the detector. In the measuring process we kept the source holder always fixed and we moved the detectors placing them at different distances. The error on the positioning of the detectors is estimated to be 2 mm. In order to work the detectors must be connected to the power supply: we use the two inputs present in the preamplifier to connect the detector to the high voltage unit and to the low voltage one. The preamplifier had also two output connectors: we always used the anodic one to read the signal. Firstly, the signal was sent to the oscilloscope so it was possible to check its shape. A signal coming directly from the anode output is shown in Figure 9b. Then, the anodic output was directly connected to the V1730 CAEN board to be processed. The board is coupled to the CoMPASS software, which we used during the entire acquisition. If not specified otherwise, all the acquisitions were done using the DPP-PHA mode.



(a) Experimental set up adopted in the first part of the experiment



(b) Signal coming from the detector's anode read directly on the oscilloscope

Figure 9 9a shows the experimental set up adopted in the first part of the experiment; in the photo the two  $\text{LaBr}_3(\text{Ce})$  detectors are mounted. 9b shows the signal coming directly from the anode of the detector.

### 2. Adopted notation on the errors

In this part of the report for improving the readability we adopted the following conventions:

- The energy of the gamma rays emitted by the sources in the following are labeled just as 1275 keV, 1172 keV, 1333 keV and 662 keV. Although the error is not indicated, it is taken into account in the analysis.
- The error on the positioning of the detectors is assumed to be 2 mm; in the following also this error is not reported but it is taken into account.

### 3. Energy calibration

In order to study the behavior of the system it is necessary to calibrate the detectors in energy. This procedure is done by acquiring a spectrum for each detector with the two sources of  $^{22}\text{Na}$  and  $^{60}\text{Co}$  in place (positioned above a plastic cylinder).

The spectra acquired in this way present 4 well visible peaks: 2 originated from the  $^{22}\text{Na}$  decay and 2 from the  $^{60}\text{Co}$  decay (in addition to the background spectrum).

The detectors are assumed to work in linear regime, so the correspondence between channel number and energies is expected to follow the linear relation:

$$E_\gamma = m \cdot N_{\text{channel}} + q$$

In order to obtain the values of the parameters  $m$  and  $q$ , a linear fit of the pairs  $(N_{\text{channel}}, E_\gamma)$  is performed. The channel number  $N_{\text{channel}}$  is obtained taking the mean of Gaussian fits of all the peaks of interest. The mean values  $N_{\text{channel}}$  are reported in Table 1, while the calibration parameters are reported in Table 2. The linear fits are displayed in Figure 10.

channel	$E_\gamma$ [keV]	$N_{\text{channel}_{LaBr}}$ [ch]	$N_{\text{channel}_{CeBr}}$ [ch]
$ch_0$	511	$686.75 \pm 0.07$	$1975.9 \pm 0.2$
	1173	$1570.8 \pm 0.3$	$4570.1 \pm 0.3$
	1275	$1707.1 \pm 0.2$	$4991.4 \pm 0.8$
	1333	$1782.8 \pm 0.2$	$5199.8 \pm 0.3$
$ch_1$	511	$716.10 \pm 0.07$	$2081.4 \pm 0.2$
	1173	$1650.6 \pm 0.3$	$4790.0 \pm 0.3$
	1275	$1799.2 \pm 0.2$	$5231.9 \pm 0.7$
	1333	$1880.0 \pm 0.4$	$5445.4 \pm 0.3$

Table 1 Values of the mean obtained from the Gaussian fit of the full energy peaks of  $^{22}\text{Na}$  and  $^{60}\text{Co}$  decays.  $N_{\text{channel}_{LaBr}}$  refers to the means obtained for the  $\text{LaBr}_3(\text{Ce})$  detectors, while  $N_{\text{channel}_{CeBr}}$  refers to the ones obtained for the  $\text{CeBr}_3$  detectors.

channel	$m_{LaBr}$ [keV/ch]	$q_{LaBr}$ [keV]	$m_{CeBr}$ [keV/ch]	$q_{CeBr}$ [keV]
$ch_0$	$0.7490 \pm 0.0001$	$-34 \pm 0.1$	$0.25485 \pm 0.00002$	$7.52 \pm 0.09$
$ch_1$	$0.7059 \pm 0.0001$	$5.6 \pm 0.1$	$0.24413 \pm 0.00002$	$2.91 \pm 0.09$

Table 2 Values of the calibration parameters of  $ch_0$  and  $ch_1$ . As in Table 1, the subscripts refer to the  $\text{LaBr}_3(\text{Ce})$  and  $\text{CeBr}_3$  detectors.

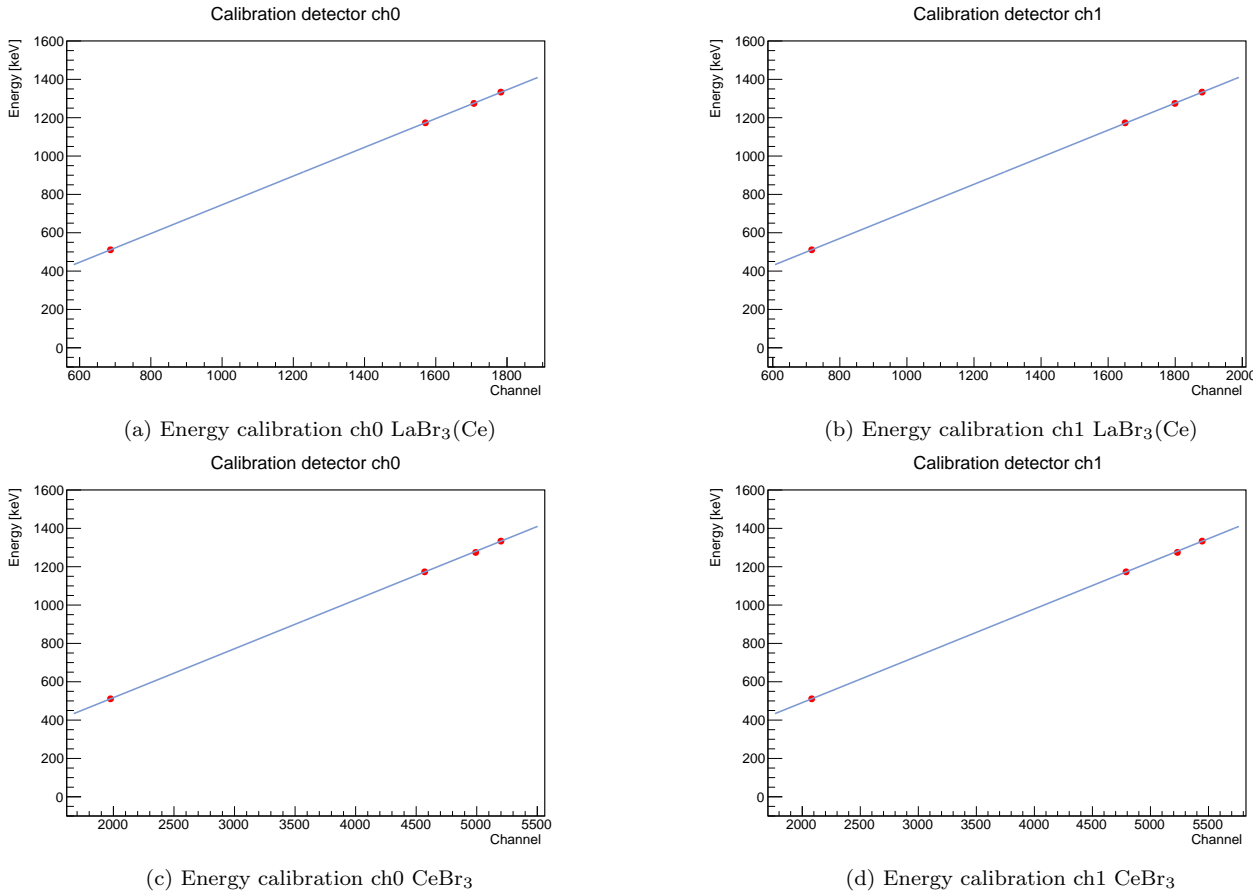


Figure 10 In 10a it is displayed the energy calibration for the ch0 LaBr<sub>3</sub>(Ce) detector, 10b shows the energy calibration for the ch1 LaBr<sub>3</sub>(Ce) detector, 10c the energy calibration for the ch0 CeBr<sub>3</sub> detector and 10d the energy calibration for the ch1 CeBr<sub>3</sub> detector.

To validate the assumption of the detector's linear behavior in the energy region of interest, we exploited the variable

$$t = \frac{\rho\sqrt{N-2}}{\sqrt{1-\rho^2}}$$

that follows the t-Student statistics with N-2 degrees of freedom. N is the number of data points used for the linear fit. Table 3 shows the values of the parameters  $\rho$ , N, t and the percentage at which it is possible to reject hypothesis that the data are not correlated. From the values obtained, it is possible to affirm that the hypothesis of not linear correlation is false with 99% confidence level for all the four linear fits performed to calibrate the detectors.

channel	$\rho_{LaBr}$	$N_{LaBr}$	$t_{LaBr}$	$\%_{LaBr}$	$\rho_{CeBr}$	$N_{CeBr}$	$t_{CeBr}$	$\%_{CeBr}$
ch <sub>0</sub>	0.999999	4	999.999	99%	0.99998	4	208.51	99%
ch <sub>1</sub>	0.999992	4	353.6	99%	0.99997	4	182.57	99%

Table 3 Parameters obtained with the t-student test; as above the subscripts refer to the two different types of detectors used: LaBr<sub>3</sub>(Ce) and CeBr<sub>3</sub>.

#### 4. Width calibration

In addition to the energy calibration, the width calibration is performed. This allows to understand how the FWHM of the full energy peaks of <sup>22</sup>Na and <sup>60</sup>Co changes with increasing energy. What is more, the width of the peaks plays a crucial role in measuring the peak area and in the peak fit procedure. A Gaussian fit is performed on the 4 full energy peaks and the  $\sigma$  of the Gaussian is used to calculate the FWHM as FWHM= $\sigma \cdot 2\sqrt{2 \ln 2}$ . In Table 4

are reported the values of  $\sigma$  for ch0 and ch1 of both the LaBr<sub>3</sub>(Ce) and CeBr<sub>3</sub> detectors; the detectors are fixed at a distance of 18 cm from the <sup>22</sup>Na and <sup>60</sup>Co sources.

channel	$E_\gamma$ [keV]	$\sigma_{LaBr}$ [keV]	$\sigma_{CeBr}$ [keV]
<i>ch<sub>0</sub></i>	511	11.5 ± 0.1	10.93 ± 0.06
	1173	15.2 ± 0.1	17.40 ± 0.09
	1275	15.3 ± 0.3	17.4 ± 0.3
	1333	15.4 ± 0.1	18.01 ± 0.08
<i>ch<sub>1</sub></i>	511	12.2 ± 0.1	10.84 ± 0.06
	1173	17.3 ± 0.2	16.62 ± 0.08
	1275	17.9 ± 0.3	17.0 ± 0.2
	1333	18.3 ± 0.2	16.93 ± 0.09

Table 4 Values of  $\sigma$  obtained from the Gaussian fit of the full energy peaks of <sup>22</sup>Na and <sup>60</sup>Co. The subscript refers to the type of detector.

Differently from the energy calibration, the trend of the FWHM dependency on the energy is not known a priori and the calibration should be performed fitting the data with a certain function. According to [1] the following functions are expected to best fit the experimental data:

- Linear function  $FWHM = a + bE$ ;
- Debertin and Helmer function  $FWHM = \sqrt{a^2 + b^2 E}$ ;
- Square root quadratic function  $FWHM = \sqrt{a^2 + b^2 E + c^2 E^2}$ .

To determine the best fitting function for our data, we proceeded in the following way:

- Fitted each data set ( $E_\gamma$ , FWHM) with  $\sigma$  from Table 4 with all the three functions listed above
- Checked the residuals for each fit
- Determined the best fitting function in each case.

From this analysis it turned out that the best fitting function is the Debertin and Helmer function function in all four cases. Figure 11 shows the data fitted with the Debertin and Helmer function and Figure 12 shows the residuals of the fits. In Table 5 we report the parameters obtained with the fits. As it is possible to see from both the graphs and the obtained parameters, the calibration of the FWHM is not completely satisfactory. A rough trend can be extracted, but the large gap between the 511 keV gamma peak and the other three full energy peaks is large. A possibility to improve the width calibration might be the usage of additional radioactive sources to increase the number of full energy peaks in the uncovered region between 511 keV and 1173 keV. In this way it would be possible to extract the trend of the FWHM growth in a more precise manner.

channel	$a$ [keV]	$b$ [keV <sup>1/2</sup> ]	$\chi^2$	$\rho$
<i>ch<sub>0</sub>LaBr<sub>3</sub>(Ce)</i>	18.8 ± 0.6	0.86 ± 0.01	13.3	0.991
<i>ch<sub>1</sub>LaBr<sub>3</sub>(Ce)</i>	13 ± 1	1.12 ± 0.02	0.02	0.9995
<i>ch<sub>0</sub>CeBr<sub>3</sub></i>	0 ± 1	1.162 ± 0.003	44.6	0.993
<i>ch<sub>1</sub>CeBr<sub>3</sub></i>	5 ± 1	1.106 ± 0.008	38.8	0.991

Table 5 Values of the parameters a and b obtained from the fit of the FWHM as a function of the energy using a Debertin and Helmer function. The  $\chi^2$  and the  $\rho$  correlation factor are also reported.

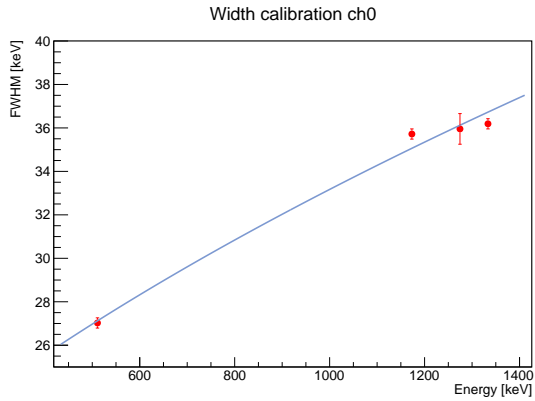
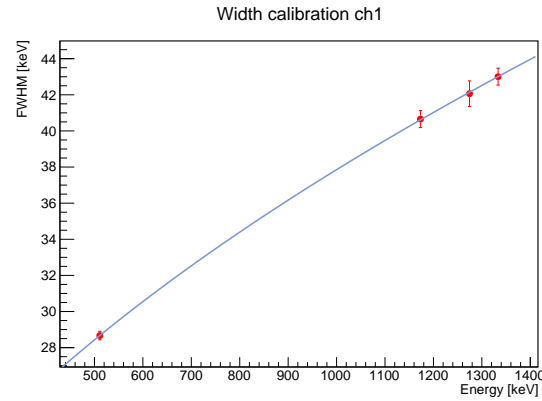
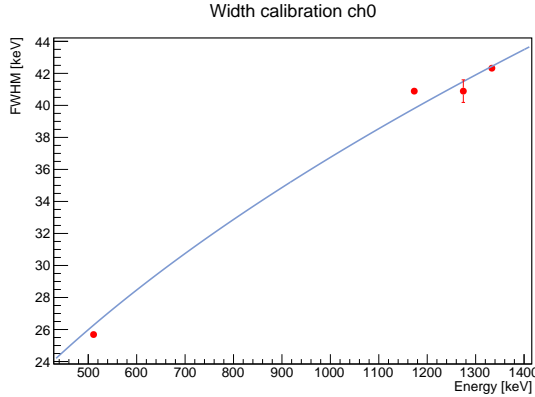
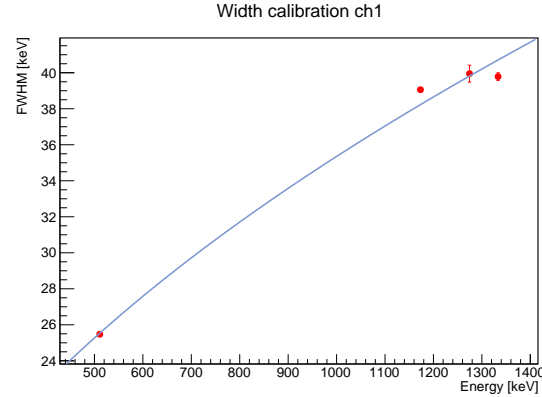
(a) Width calibration ch0 LaBr<sub>3</sub>(Ce)(b) Width calibration ch1 LaBr<sub>3</sub>(Ce)(c) Width calibration ch0 CeBr<sub>3</sub>(d) Width calibration ch1 CeBr<sub>3</sub>

Figure 11 11a shows the FWHM as a function of the energy fitted with a Debertin and Helmer function for the ch0 LaBr<sub>3</sub>(Ce), 11b for the ch1 LaBr<sub>3</sub>(Ce), 11c for the ch0 CeBr<sub>3</sub>, 11b for the ch1 ch0 CeBr<sub>3</sub>.

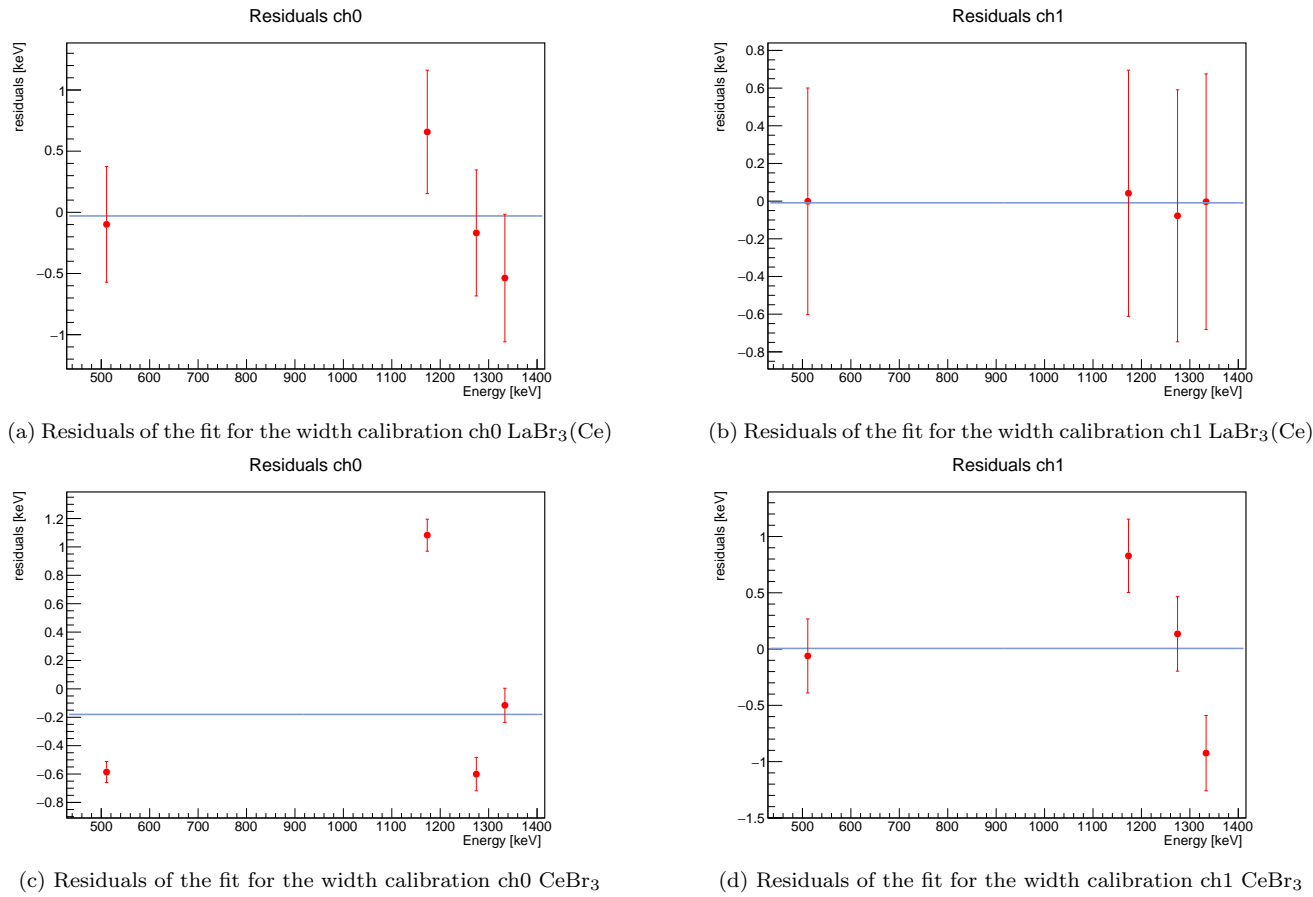


Figure 12 12a shows the residuals of the fitting with the Debertin and Helmer function for the ch0 LaBr<sub>3</sub>(Ce), 12b for the ch1 LaBr<sub>3</sub>(Ce), 12c for the ch0 CeBr<sub>3</sub>, 12b for the ch1 ch0 CeBr<sub>3</sub>.

## 5. Intrinsic activity of the LaBr<sub>3</sub>(Ce) detectors

After the calibration procedure, the intrinsic background of the detectors was assessed. To do this, the sources were removed and several acquisitions were taken changing the relative position of the detectors. Figure 13 shows the spectra acquired for the two detectors both placed at a distance of 48 cm from the central point. The intrinsic activity of LaBr<sub>3</sub>(Ce) detectors is mainly due to the nuclei of <sup>138</sup>La and <sup>227</sup>Ac and it is expected to be of about 1-2 counts/cm<sup>3</sup> · s [2]. <sup>138</sup>La is a constituent of the crystal and it is radioactive with two possible decay modes:

- It decays through electron capture in <sup>138</sup>Ba emitting a gamma-ray with an energy of 1436 keV; in coincidence with the gamma-ray also an X-ray of 32 keV is emitted. As a consequence, the peak at 1436 keV is expected to present a double structure: a peak at 1436 keV and a peak at the sum of the energies of the gamma-ray and of the X-ray. The visibility of the double peak structure strongly depends on the detector resolution in energy. With the detectors used in this experiment we were not able to have an energy resolution good enough to allow a clear distinction of the double peak structure.
- It decays via  $\beta^-$  emitting a gamma-ray with an energy of 789 keV; in coincidence with the gamma-ray also an electron with end point energy of 255 keV is emitted.

Another radioactive contribution arises from the presence of <sup>227</sup>Ac, which is the chemical analogue of lanthanum. The contribution from <sup>227</sup>Ac can be divided into two components:

- The  $\beta$  decays of <sup>211</sup>Pb and <sup>207</sup>Tl (nuclei present in the decay chain of <sup>227</sup>Ac) gives rise to a  $\beta$  continuum up to 1400 keV.
- The  $\alpha$  decay chain of <sup>227</sup>Ac populates the nuclei <sup>227</sup>Th, <sup>223</sup>Ra, <sup>219</sup>Rn, <sup>215</sup>Po, <sup>211</sup>Bi, which in turn decay emitting  $\alpha$  particles. This contributes to the region of the spectrum comprised between about 1500 keV and 2750 keV.

It is important to notice that the energy calibration of the spectra was done considering the energy of gamma-rays. Since the interaction of the  $\alpha$  particles with matter is different from that of a gamma-ray, the energy positions of the  $\alpha$  in the spectra are not at the energy of their emission energy, but at a lower energy.

Finally, the background spectra have also an environmental contribution, due to the presence in the environment of the nucleus of  $^{40}\text{K}$ . The decay of  $^{40}\text{K}$  is responsible for the gamma line at 1461 keV.

As it is possible to see from Figure 13, the detector in ch0 acquired the spectra with better resolution. In fact, several attempts were made to improve the resolution of detector ch1 (either changing the CAEN acquisition settings or the detector high voltage), but it did not reach the same performances of detector ch1.

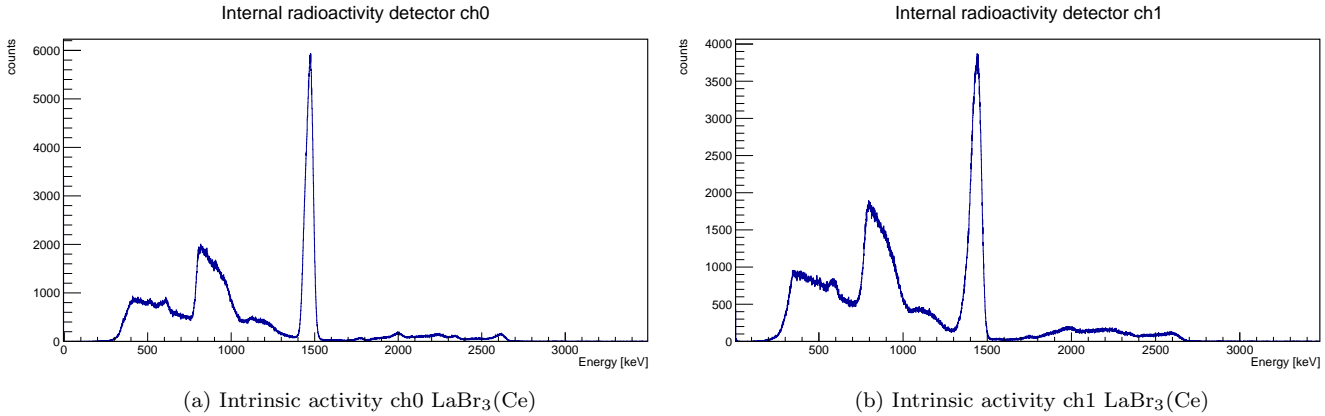


Figure 13 In 13a it is displayed the intrinsic radioactivity for the ch0  $\text{LaBr}_3(\text{Ce})$  detector, while in 13b it is displayed the intrinsic radioactivity for the ch1  $\text{LaBr}_3(\text{Ce})$  detector.

## 6. Background evaluation:

To proceed to the characterization of the detectors, we mounted the  $\text{LaBr}_3(\text{Ce})$  detectors and acquired spectra at different distances. In this procedure we firstly acquired with the  $^{22}\text{Na}$  source in place and then we repeated the procedure with the  $^{60}\text{Co}$  source. We kept the acquisition going until the net counts in the full energy peaks of the gamma rays emitted by the sources were about 10 000. This allowed to have an uncertainty of about 1%.

The same procedure was then repeated for the  $\text{CeBr}_3$  detectors. In this subsection and in the following ones we analyze these data.

In order to calculate the signal-to-noise ratio and the efficiency it is necessary to separate the background contribution from the signal contribution of the full energy peaks. In order to do this, we subtracted the background using three different methods:

- Trapezoid method: with this method one needs to find the mean values of the left  $m_L$  and right  $m_R$  background regions. This is done on a range of 50 bins before the last point of the left background  $s_M$  for the  $m_L$  value and on a range of 50 bins after the last point of the right background  $d_m$  for the  $m_R$  value. Then the background subtraction is done by subtracting from the integral under the peak the following quantity:

$$\frac{(m_L + m_R)(d_m - s_M)}{2}$$

Figure 14 shows the peak and the region subtracted using the trapezoid method.

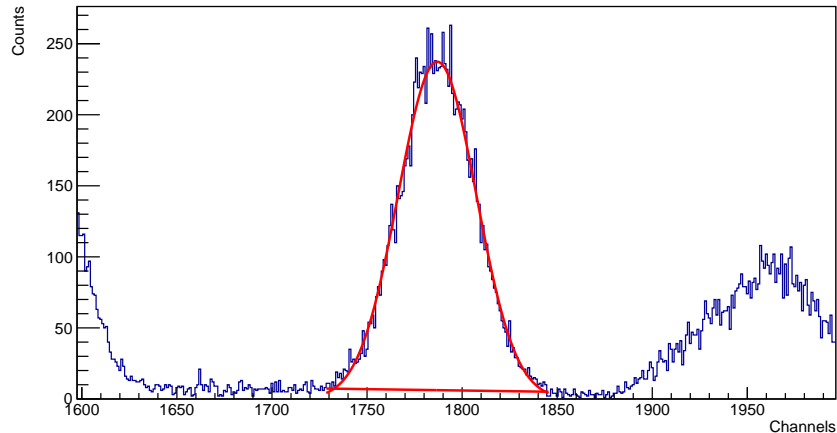


Figure 14 Trapezoid background subtraction for 1333 keV peak of CH0 of the at LaBr<sub>3</sub>(Ce) detector placed at 18 cm from the source. The x axis in in channels.

- Step-function method: at first one needs to take into consideration the background on the left and on the right of the peak and to evaluate each mean value  $m_L$ ,  $m_R$ . Thanks to a Gaussian fit it is possible to estimate the mean of the peak.

To subtract the background to the peak counts one has to take the value of  $m_L$  and to extend it until the mean value of the peak. The same has to be done with  $m_R$ . This procedure allows to generate the step function that is subtracted. Figure 15 shows the peak and the region subtracted using the step function method.

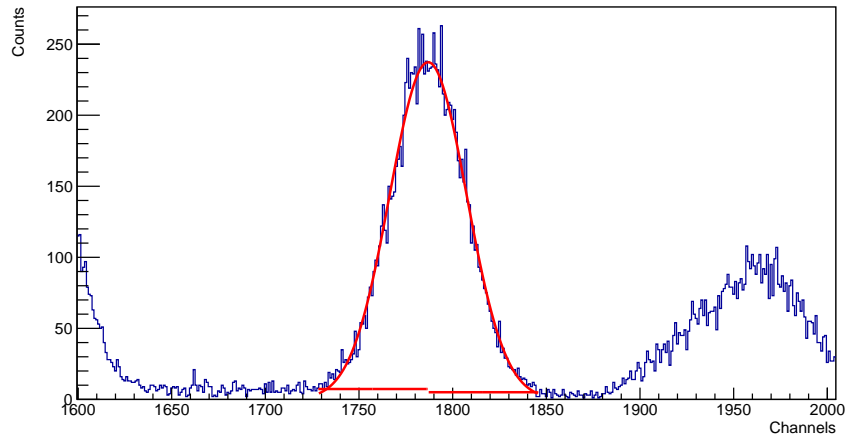


Figure 15 Step function background subtraction for 1333 keV peak of CH0 of the at LaBr<sub>3</sub>(Ce) detector placed at 18 cm from the source. The x axis in in channels.

- Fermi function: after the estimation of  $m_L$  and  $m_R$  and the evaluation of the mean value of the peak it is possible to interpolate a Fermi function that has the mean value as inflection.

$$f(x) = \frac{a}{1 + e^{x-b}} + c$$

Figure 16 shows the peak and the region subtracted using the Fermi function method.

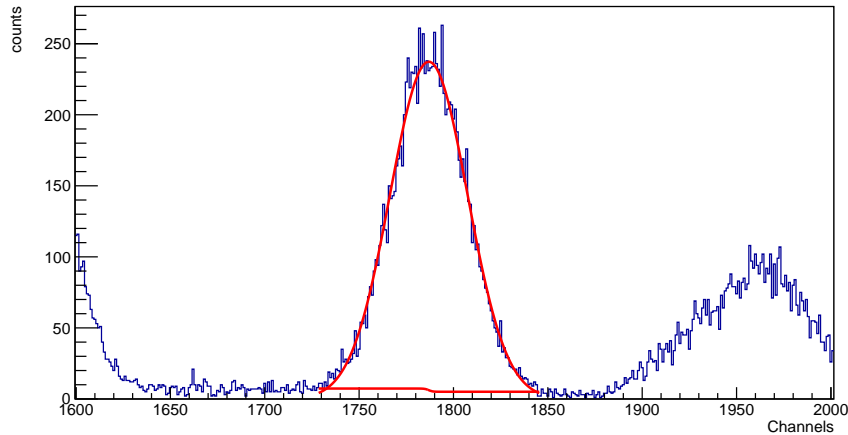


Figure 16 Fermi function background subtraction for 1333 keV peak of CH0 of the at LaBr<sub>3</sub>(Ce) detector placed at 18 cm from the source. The x axis in in channels.

Firstly we calculated the background for the four full energy peaks acquired with the LaBr<sub>3</sub>(Ce) detectors placed at different distances and with the three methods we obtained consistent results. In particular, the step function and the Fermi function methods gave identical or very similar results. In order to decide which method to use in the following analysis we made a code to calculate the background varying randomly, within a range of 50 bins, the values of the last point of the left and right background,  $s_m$  and  $d_m$  respectively. The random generation of the two extremes is run 100 times and we noticed that the net number of counts under the peak does not change significantly. Increasing the number of the range of  $s_m$  and  $d_m$  up to 100 we observed that the net counts start changing in the same way for all the three methods.

We choose then the Fermi subtraction method to calculate the background for all the peaks in the following analysis.

## 7. Signal to noise ratio

After the energy and width calibration, we placed the <sup>22</sup>Na source equidistant from the two LaBr<sub>3</sub>(Ce) detectors. The detectors are positioned at the following distances d=13, 18, 23, 28, 38 and 48 cm.

Then we changed the source to <sup>60</sup>Co and acquired with the LaBr<sub>3</sub>(Ce) detectors placed at d=13, 18, 23, 28, 38 and 48 cm.

We repeated the same acquisition also for the CeBr<sub>3</sub> detectors. The distances of the detectors are the same in the <sup>22</sup>Na measurement, while we acquired using the <sup>60</sup>Co source only with the detectors placed at d=5 and 18 cm.

In the characterization of the detectors the signal to noise ratio is an important parameter that allows to quantify the ability of a detector to distinguish a signal from the background. We calculated the signal to noise ratio as

$$\frac{(Counts_{Peak}) - (Counts_{Background})}{Counts_{Background}}$$

The results obtained for the four full energy peaks at 511 keV, 1275 keV, 1173 keV and 1333 keV detected with all four detectors are reported in Tables 6, 7, 8 and 9. Figure 17 shows the signal-to-noise ratio for the 511 keV and 1275 keV peaks, while Figure 18 shows the signal-to-noise for the 1173 keV and 1333 keV peaks.

channel	d (cm)	Signal-noise <sub>511</sub>	Signal-noise <sub>1275</sub>
<i>ch<sub>0</sub></i>	13	7.5 ±0.2	8.8 ±0.1
	18	5.8 ±0.2	6.4 ±0.2
	23	4.6 ±0.1	5.02 ±0.09
	28	3.2 ±0.1	3.58 ±0.06
	38	2.27 ±0.07	2.29 ±0.05
	48	1.32 ±0.04	1.55 ±0.03
<i>ch<sub>1</sub></i>	13	6.2 ±0.1	8.7 ±0.1
	18	4.2 ±0.2	6.2 ±0.2
	23	2.75 ±0.07	4.64 ±0.08
	28	1.99 ±0.07	3.55 ±0.08
	38	1.29 ±0.04	2.20 ±0.04
	48	0.71 ±0.03	1.45 ±0.03

Table 6 Ratio signal-noise of the <sup>22</sup>Na peaks with the LaBr<sub>3</sub>(Ce) scintillators.

channel	d (cm)	Signal-noise <sub>1173</sub>	Signal-noise <sub>1333</sub>
<i>ch<sub>0</sub></i>	13	8.9 ±0.2	22.2 ±0.8
	18	8.3 ±0.2	15.9 ±0.6
	23	6.4 ±0.2	14.3 ±0.5
	28	5.6 ±0.1	11.4 ±0.4
	38	3.93 ±0.08	7.6 ±0.2
	48	2.91 ±0.05	5.3 ±0.1
<i>ch<sub>1</sub></i>	13	5.9 ±0.1	5.5 ±0.1
	18	5.0 ±0.1	4.13 ±0.09
	23	4.11 ±0.09	3.52 ±0.07
	28	3.75 ±0.07	3.07 ±0.06
	38	2.81 ±0.05	1.89 ±0.03
	48	2.17 ±0.04	1.53 ±0.03

Table 7 Ratio signal-noise of the <sup>60</sup>Co decay peaks detected with the LaBr<sub>3</sub>(Ce) scintillators.

channel	d (cm)	Signal-noise <sub>511</sub>	Signal-noise <sub>1275</sub>
<i>ch<sub>0</sub></i>	13	7.2 ±0.2	9.2 ±0.2
	18	5.1 ±0.2	8.2 ±0.2
	23	3.3 ±0.1	7.0 ±0.2
	28	1.99 ±0.07	6.1 ±0.1
	38	1.98 ±0.07	4.68 ±0.09
	48	1.40 ±0.06	3.56 ±0.07
<i>ch<sub>1</sub></i>	13	7.4 ±0.2	7.8 ±0.1
	18	4.9 ±0.2	6.8 ±0.1
	23	3.3 ±0.1	5.9 ±0.1
	28	2.68 ±0.09	5.5 ±0.1
	38	1.76 ±0.06	4.35 ±0.08
	48	1.03 ±0.05	3.45 ±0.06

Table 8 Ratio signal-noise of the <sup>22</sup>Na peaks with the CeBr<sub>3</sub> scintillators.

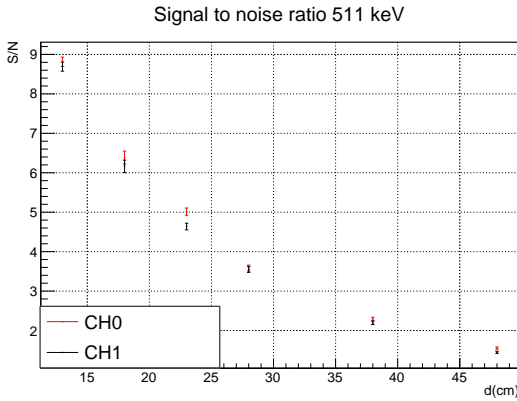
channel	d (cm)	Signal-noise <sub>1173</sub>	Signal-noise <sub>1333</sub>
<i>ch<sub>0</sub></i>	5	8.02 ±0.09	26.5 ±0.6
	18	7.3 ±0.1	22.8 ±0.6
<i>ch<sub>1</sub></i>	5	8.01 ±0.09	20.5 ±0.4
	18	7.4 ±0.1	22.8 ±0.6

Table 9 Ratio signal-noise of the <sup>60</sup>Co decay peaks detected with the CeBr<sub>3</sub> scintillators.

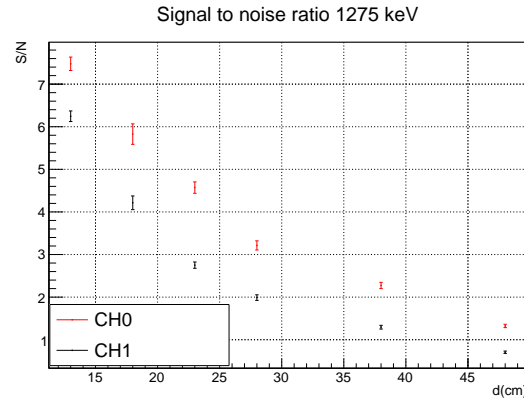
As it is possible to see, the signal-to-noise ratio is better at smaller distances. This is due to the fact that at smaller

distances the solid angle covered by the detector is larger and so there is a higher collection of events. The signal-to-noise ratio has also a strong dependence on the energy and on the structures of the spectrum. In particular, the signal-to-noise ratio increases with energy since the contribution of beta continuum, in our case, is lower at higher energy. An additional contribution arises from the internal radioactivity of the detectors: an higher internal background lowers the signal-to-noise ratio.

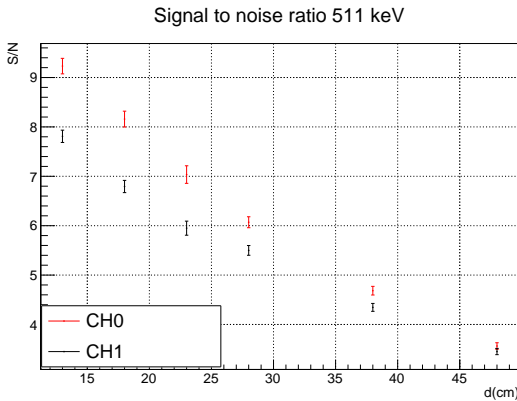
As it was already pointed out in the previous Sections, it is possible to notice that the LaBr<sub>3</sub>(Ce) ch1 detector has a performance which is lower respect to ch0.



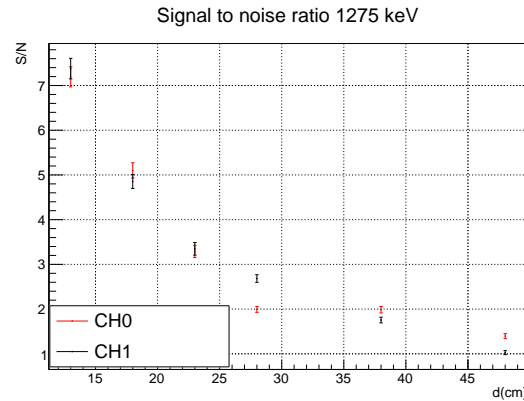
(a) S/N ratio vs distance for the 511 keV peak in LaBr<sub>3</sub>(Ce) detectors.



(b) S/N ratio vs distance for the 1275 keV peak in LaBr<sub>3</sub>(Ce) detectors.



(c) S/N ratio vs distance for the 511 keV peak in CeBr<sub>3</sub> detectors



(d) S/N ratio vs distance for the 1275 KeV peak in CeBr<sub>3</sub> detectors.

Figure 17 Signal-to-noise ratio at various distances for the 511 keV and 1275 keV peaks.

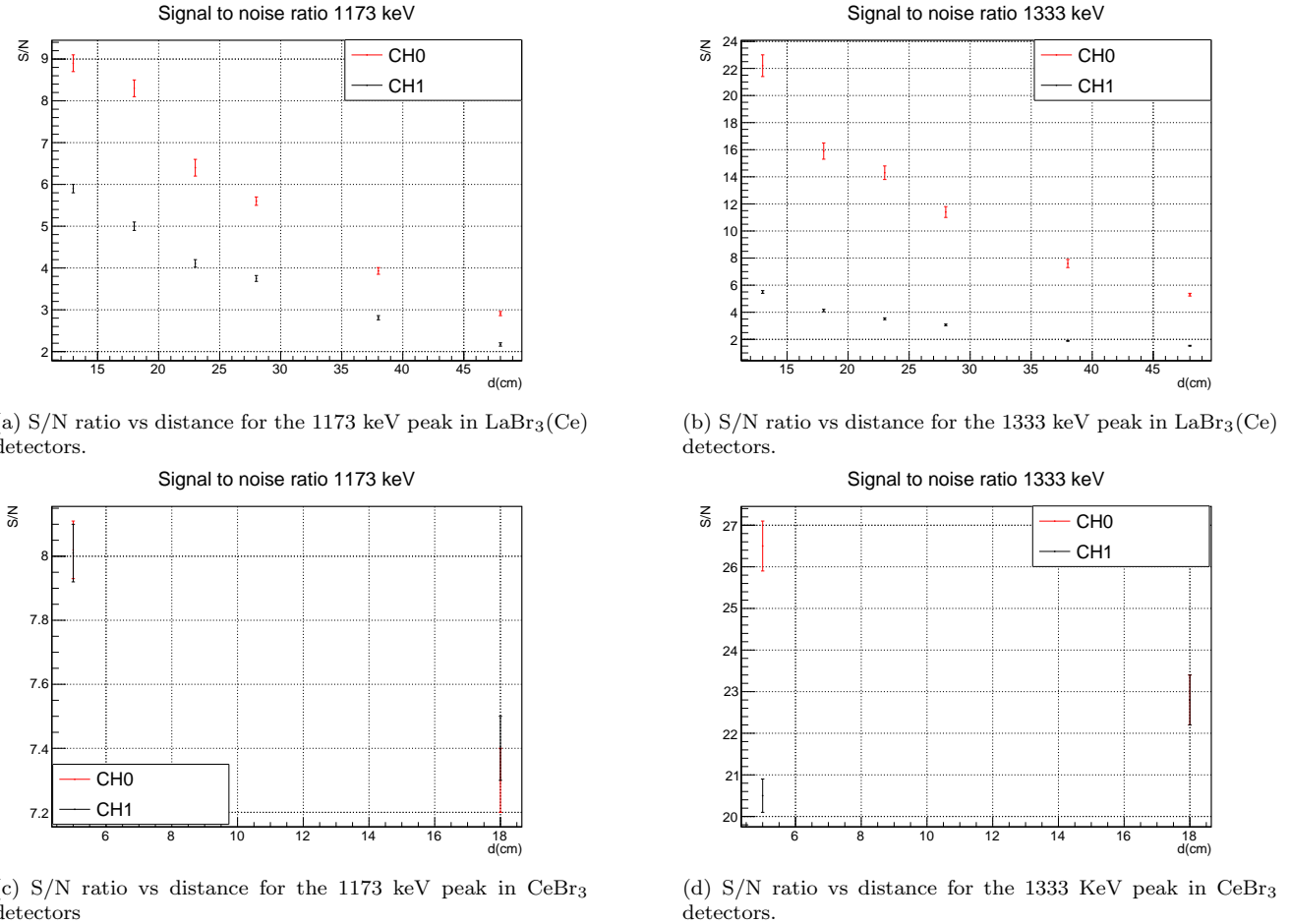


Figure 18 Signal-to-noise ratio at various distances for the 1173 keV and 1333 keV peaks.

## 8. Study of the coincidences

After the data acquisition a macro is made in order to obtain the number of the couples of 511 keV  $\gamma$ -rays in coincidence coming from the positron annihilation (so from the  $\beta^+$  decay of the  $^{22}\text{Na}$  nucleus).

The macro made for the coincidences of the two gamma rays of 511 keV energy selects the data with energy under the peak within  $3\sigma$  and makes an histogram of the temporal differences of these events, from which the time-threshold for the coincidences can be derived. This time threshold was estimated to be the value where the temporal distribution goes to zero, as seen in Fig. 19 and set to 30000 ps.

The coincident events are selected as the ones within the energy threshold given above and within the time-threshold.

For the LaBr<sub>3</sub>(Ce) detectors it is also possible to take into account for the coincidences between one 511 keV gamma ray and the couple 511 keV gamma and 1275 keV gamma, the latter considered simultaneous to the  $\beta$  decay and subsequent positron annihilation. The net counts obtained with this method for the LaBr<sub>3</sub>(Ce) detectors are reported in Table 10; the net counts obtained for the CeBr<sub>3</sub> detector are reported in Table 11.

In Fig. 20 and 22 are reported the number of coincidences under the 511 keV peak as a function of the energy taken at a distance of 48 cm for LaBr<sub>3</sub>(Ce) and CeBr<sub>3</sub> detectors respectively. In Fig. 21 and 23 we reported the number of coincidences as a function of the energy of both the two detectors (ch0 and ch1) for LaBr<sub>3</sub>(Ce) and CeBr<sub>3</sub> detectors respectively.

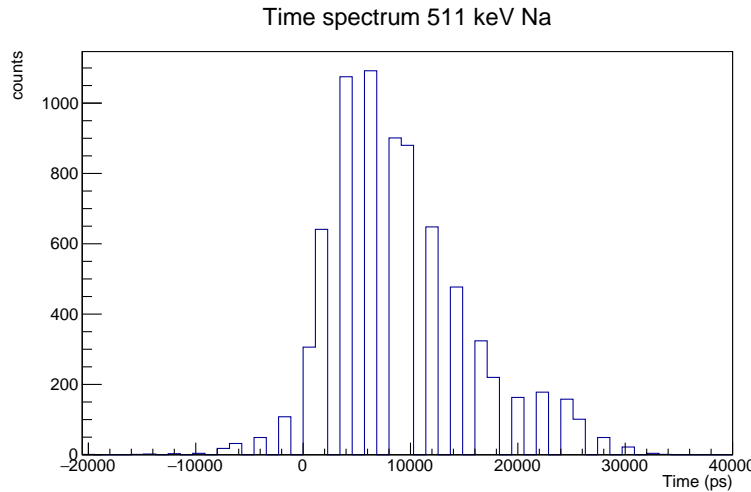


Figure 19 Temporal histogram for the LaBr<sub>3</sub>(Ce) detector at a distance of 48cm.

<b>d (cm)</b>	<b>N<sub>counts</sub> 511 keV</b>	<b>N<sub>counts</sub> (511+1275) keV</b>
13	34600 ±200	35 200 ±200
18	7270 ±90	7310 ±90
23	12100 ±100	12 100 ±100
28	7300 ±90	7320 ±90
38	6810 ±80	6820 ±80
48	7430 ±90	7440 ±90

Table 10 Number of the coincidences of the 511 keV peak and of the coincidences of the 511 keV peak considering also the contribution of sum peak 511+1275 keV. The detector used were the LaBr<sub>3</sub>(Ce) ones.

<b>d (cm)</b>	<b>N<sub>counts</sub> 511 keV</b>
13	6990 ± 80
18	4530 ± 70
23	2450 ± 50
28	3730 ± 60
38	3200 ± 60
48	2790 ± 50

Table 11 Number of the coincidences of the 511 keV peak with Na source and CeBr<sub>3</sub> detectors.

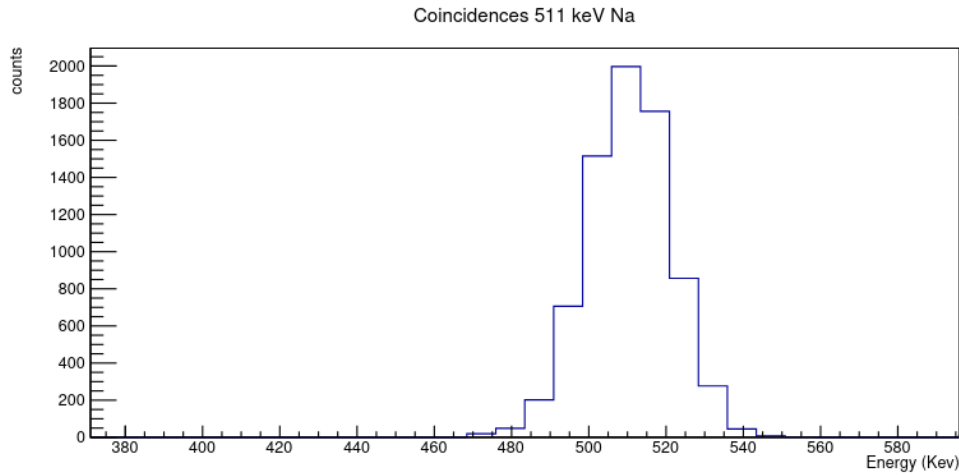


Figure 20 Counts of the coincidences for the 511 keV peak as a function of the energy for the LaBr<sub>3</sub>(Ce) detector at a distance of 48cm.

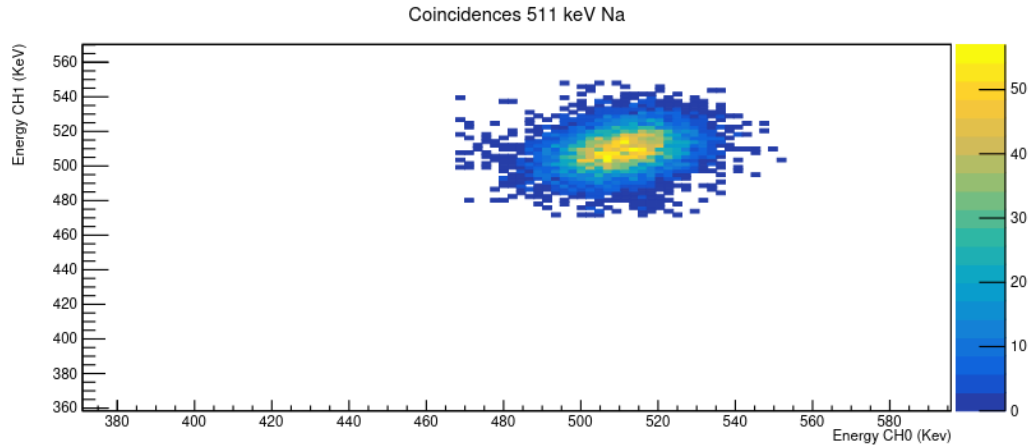


Figure 21 Coincidences between the 2 channels of the 511 keV for the LaBr<sub>3</sub>(Ce) detector at a distance of 48 cm.

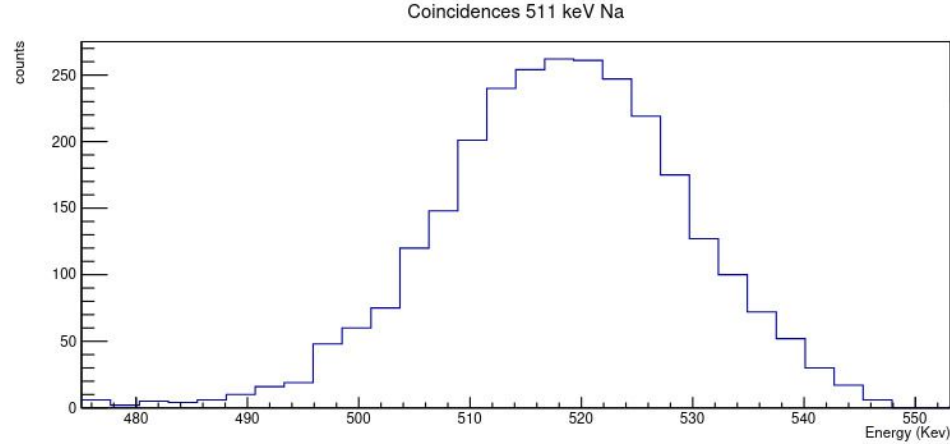


Figure 22 Counts of the coincidences for the 511 keV peak as a function of the energy for the CeBr<sub>3</sub> detector at a distance of 48cm.

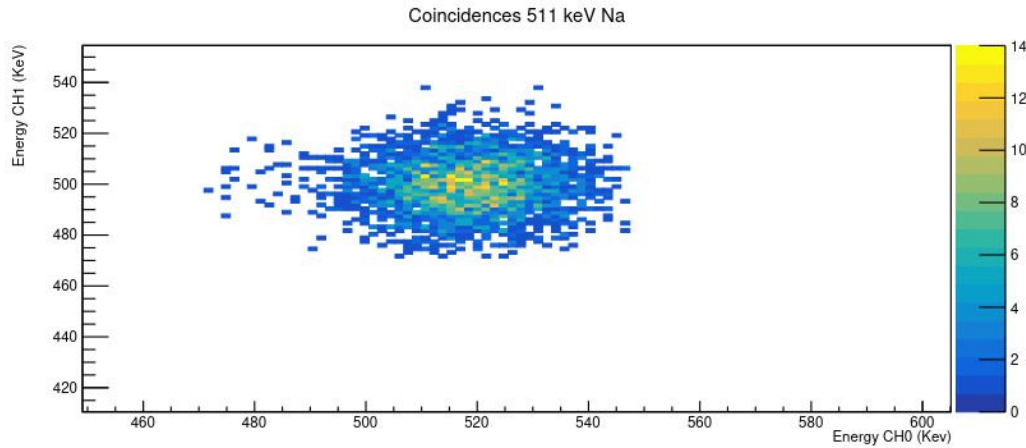


Figure 23 Coincidences between the 2 channels of the 511 keV for the CeBr<sub>3</sub> detector at a distance of 48 cm.

## 9. Efficiency

To characterize a detector it is important to determine its efficiency, because it quantifies its ability to detect a gamma ray which interacts and convert it into a signal. Efficiency is a function of several parameters, such as the type of detector, its size, the distance from the source.

In the following we calculated the efficiency using two methods: the first one uses the integral of the full energy peak and the second one exploits coincident events.

### A. Efficiency with integral under the peaks

From the law of nuclear decay, we know that the following relation for the activity holds

$$A(t) = A_0 e^{-t\lambda}$$

where  $A(t)$  is the activity at the time  $t$ ,  $A_0$  the one at the initial time  $t_0$  and  $\lambda$  is the decay constant. Knowing that on the July 9, 2010 the <sup>60</sup>Co activity was 443 kBq and the <sup>22</sup>Na activity on September 1, 2011 was 402 kBq (with an estimated uncertainty of 1%) one can estimate the current activities:  $23.4 \pm 0.2$  kBq for the <sup>22</sup>Na source and  $93.6 \pm 0.9$  kBq for the <sup>60</sup>Co one. Using the information on the activity, it is then possible to calculate the efficiency  $\epsilon$  for the four full energy peaks of <sup>22</sup>Na and <sup>60</sup>Co

$$\epsilon = \frac{p_c - b}{A(t) \cdot t_a \cdot BR}$$

where  $p_c$  is the counts under the considered peak,  $b$  the relative background (that is calculated with the Fermi function),  $t_a$  is the acquisition time and  $BR$  the branching ratio.

In Tables 12, 13, 14 and 15 we report the calculated efficiencies for the full energy peaks at 511 keV and 1275 keV of the <sup>22</sup>Na source for both the LaBr<sub>3</sub>(Ce) and CeBr<sub>3</sub> detectors. In Tables 16, 17, 18, 19 we report the calculated efficiencies for the full energy peaks at 1173 keV and 1333 keV of the <sup>22</sup>Na source for both the LaBr<sub>3</sub>(Ce) and CeBr<sub>3</sub> detectors.

channel	d (cm)	(c $\pm \sigma_c$ )	$\epsilon \pm \sigma_\epsilon$
<i>ch<sub>0</sub></i>	13	56 900 $\pm 300$	0.0242 $\pm 0.0003$
	18	11 700 $\pm 100$	0.0143 $\pm 0.0002$
	23	19 400 $\pm 200$	0.0096 $\pm 0.0001$
	28	11 600 $\pm 100$	0.0067 $\pm 0.0001$
	38	10 900 $\pm 100$	0.00392 $\pm 0.00006$
	48	12 000 $\pm 200$	0.00260 $\pm 0.00004$
<i>ch<sub>1</sub></i>	13	56 700 $\pm 300$	0.0241 $\pm 0.0003$
	18	11 400 $\pm 100$	0.0139 $\pm 0.0002$
	23	18 500 $\pm 200$	0.0092 $\pm 0.0001$
	28	11 400 $\pm 100$	0.0065 $\pm 0.0001$
	38	10 300 $\pm 100$	0.00371 $\pm 0.00006$
	48	10 000 $\pm 200$	0.00238 $\pm 0.00004$

Table 12 Efficiency  $\epsilon$  values for the 511 keV peak for LaBr<sub>3</sub>(Ce) detectors (c stands for net counts).

channel	d (cm)	(c $\pm \sigma_c$ )	$\epsilon \pm \sigma_\epsilon$
<i>ch<sub>0</sub></i>	13	20 200 $\pm 200$	0.0086 $\pm 0.0001$
	18	4340 $\pm 80$	0.0053 $\pm 0.0001$
	23	7100 $\pm 100$	0.00353 $\pm 0.00006$
	28	4470 $\pm 90$	0.00257 $\pm 0.00006$
	38	4210 $\pm 90$	0.00152 $\pm 0.00003$
	48	4700 $\pm 100$	0.00101 $\pm 0.00003$
<i>ch<sub>1</sub></i>	13	19 600 $\pm 200$	0.0084 $\pm 0.0001$
	18	3920 $\pm 80$	0.0048 $\pm 0.0001$
	23	6200 $\pm 100$	0.00307 $\pm 0.00006$
	28	3630 $\pm 90$	0.00209 $\pm 0.00005$
	38	3320 $\pm 90$	0.00120 $\pm 0.00004$
	48	3000 $\pm 100$	0.00064 $\pm 0.00002$

Table 13 Efficiency  $\epsilon$  values for the 1275 keV peak for LaBr<sub>3</sub>(Ce) detectors (c stands for net counts).

channel	d (cm)	(c $\pm \sigma_c$ )	$\epsilon \pm \sigma_\epsilon$
<i>ch<sub>0</sub></i>	13	36 100 $\pm 200$	0.00690 $\pm 0.00008$
	18	24 300 $\pm 200$	0.00377 $\pm 0.00005$
	23	13 000 $\pm 100$	0.00247 $\pm 0.00003$
	28	22 100 $\pm 200$	0.00175 $\pm 0.00002$
	38	17 500 $\pm 200$	0.00097 $\pm 0.00001$
	48	14 900 $\pm 200$	0.000615 $\pm 0.000009$
<i>ch<sub>1</sub></i>	13	35 700 $\pm 200$	0.00681 $\pm 0.00008$
	18	24 400 $\pm 200$	0.00378 $\pm 0.00005$
	23	12 700 $\pm 100$	0.00241 $\pm 0.00003$
	28	21 300 $\pm 200$	0.00168 $\pm 0.00002$
	38	17 100 $\pm 200$	0.00095 $\pm 0.00001$
	48	15 000 $\pm 200$	0.000620 $\pm 0.000009$

Table 14 Efficiency  $\epsilon$  values for the 511 keV peak for CeBr<sub>3</sub> detectors (c stands for net counts.)

channel	d (cm)	(c $\pm \sigma_c$ )	$\epsilon \pm \sigma_\epsilon$
<i>ch<sub>0</sub></i>	13	8600 $\pm 100$	0.00165 $\pm 0.00003$
	18	5710 $\pm 90$	0.00089 $\pm 0.00002$
	23	2830 $\pm 70$	0.00054 $\pm 0.00001$
	28	3720 $\pm 90$	0.000294 $\pm 0.000007$
	38	3050 $\pm 80$	0.000169 $\pm 0.000005$
	48	2400 $\pm 80$	0.000099 $\pm 0.000003$
<i>ch<sub>1</sub></i>	13	9000 $\pm 100$	0.00171 $\pm 0.00003$
	18	6050 $\pm 90$	0.00094 $\pm 0.00002$
	23	2790 $\pm 70$	0.00053 $\pm 0.00001$
	28	4370 $\pm 90$	0.000346 $\pm 0.000008$
	38	3020 $\pm 80$	0.000168 $\pm 0.000005$
	48	2020 $\pm 80$	0.000083 $\pm 0.000003$

Table 15 Efficiency  $\epsilon$  values for the 1275 keV peak for CeBr<sub>3</sub> detectors (c stands for net counts).

channel	d (cm)	(c $\pm \sigma_c$ )	$\epsilon \pm \sigma_\epsilon$
<i>ch<sub>0</sub></i>	13	21 100 $\pm 200$	0.0081 $\pm 0.0001$
	18	12 600 $\pm 100$	0.00496 $\pm 0.00007$
	23	13 200 $\pm 100$	0.00328 $\pm 0.00005$
	28	12 700 $\pm 100$	0.00237 $\pm 0.00003$
	38	12 900 $\pm 100$	0.00139 $\pm 0.00002$
	48	12 200 $\pm 100$	0.00089 $\pm 0.00001$
<i>ch<sub>1</sub></i>	13	19 500 $\pm 200$	0.0075 $\pm 0.0001$
	18	11 900 $\pm 100$	0.00470 $\pm 0.00007$
	23	12 200 $\pm 100$	0.00302 $\pm 0.00004$
	28	12 000 $\pm 100$	0.00225 $\pm 0.00003$
	38	11 800 $\pm 100$	0.00127 $\pm 0.00002$
	48	11 600 $\pm 200$	0.00085 $\pm 0.00001$

Table 16 Efficiency  $\epsilon$  values for the 1173 keV peak for LaBr<sub>3</sub>(Ce) detectors (c stands for net counts).

channel	d (cm)	(c $\pm \sigma_c$ )	$\epsilon \pm \sigma_\epsilon$
<i>ch<sub>0</sub></i>	13	19 700 $\pm 200$	0.00754 $\pm 0.00009$
	18	11 600 $\pm 100$	0.00456 $\pm 0.00006$
	23	12 200 $\pm 100$	0.00303 $\pm 0.00004$
	28	11 800 $\pm 100$	0.00220 $\pm 0.00003$
	38	11 600 $\pm 100$	0.00125 $\pm 0.00002$
	48	10 800 $\pm 100$	0.00078 $\pm 0.00001$
<i>ch<sub>1</sub></i>	13	17 800 $\pm 200$	0.00679 $\pm 0.00009$
	18	10 200 $\pm 100$	0.00403 $\pm 0.00006$
	23	10 600 $\pm 100$	0.00262 $\pm 0.00004$
	28	9 700 $\pm 100$	0.00180 $\pm 0.00003$
	38	9 100 $\pm 100$	0.00098 $\pm 0.00002$
	48	7 900 $\pm 100$	0.00057 $\pm 0.00001$

Table 17 Efficiency  $\epsilon$  values for the 1333 keV peak for LaBr<sub>3</sub>(Ce) detectors (c stands for net counts).

channel	d (cm)	(c $\pm \sigma_c$ )	( $\epsilon \pm \sigma_\epsilon$ )
<i>ch<sub>0</sub></i>	5	68 500 $\pm 300$	0.00647 $\pm 0.00007$
	18	34 700 $\pm 200$	0.00095 $\pm 0.00001$
<i>ch<sub>1</sub></i>	5	70 500 $\pm 300$	0.00666 $\pm 0.00007$
	18	35 700 $\pm 210$	0.00098 $\pm 0.00001$

Table 18 Efficiency  $\epsilon$  values for the 1173 keV peak for CeBr<sub>3</sub> detectors (c stands for net counts).

channel	d (cm)	(c $\pm\sigma_c$ )	( $\epsilon \pm \sigma_\epsilon$ )
<i>ch<sub>0</sub></i>	5	62 580 $\pm$ 260	0.005 91 $\pm$ 0.00006
	18	32 100 $\pm$ 190	0.000 88 $\pm$ 0.00001
<i>ch<sub>1</sub></i>	5	6430 $\pm$ 270	0.006 08 $\pm$ 0.00007
	18	32 980 $\pm$ 190	0.000 91 $\pm$ 0.00001

Table 19 Efficiency  $\epsilon$  values for the 1333 keV peak for CeBr<sub>3</sub> detectors (c stands for net counts).

### B. Efficiency from Na coincidences

The efficiency for Na coincidences are calculated as the ratio between the number of coincidences under the 511 keV peak (as calculated previously in the relative section) and the expected number of coincidences  $N_{coinc,exp} = BRt_aA(t)$ , where BR is the branching ratio,  $t_a$  the acquisition time and A(t) the activity of the source.

In tables 20 and 21 are reported the efficiencies from the coincidences of the two 511 keV gamma rays for the LaBr<sub>3</sub>(Ce) and CeBr<sub>3</sub> detectors (for the LaBr<sub>3</sub>(Ce) detector also considering the coincidences between one 511 keV gamma ray and the sum of one 511 keV gamma ray and the one of 1275 keV of the gamma decay of Na).

The efficiencies obtained with this method are roughly one half the ones obtained using the method of the integral of the full energy peak. The method that exploits the coincidences allows us to remove almost completely background events; the downside of this method is that two detectors are needed. On the other hand, the method based on the integral of the full energy peak can be applied to just one detector, but it suffers issues in removing completely the background. Although we subtracted the background contributions using the Fermi function method, events not coming from the electron positron annihilation may still be present.

d (cm)	( $N_{coinc} \pm \sigma_{N_{coinc}}$ )	$\epsilon \pm \sigma_\epsilon$
13	35 200 $\pm$ 200	0.0150 $\pm$ 0.0007
18	7310 $\pm$ 90	0.0089 $\pm$ 0.0001
23	12 100 $\pm$ 100	0.005 99 $\pm$ 0.00008
28	7320 $\pm$ 90	0.004 21 $\pm$ 0.00006
38	6820 $\pm$ 80	0.002 46 $\pm$ 0.00004
48	7440 $\pm$ 90	0.001 61 $\pm$ 0.00002

Table 20 Efficiency  $\epsilon$  values from the coincidences of the two gamma rays of 511 keV for LaBr<sub>3</sub>(Ce) detectors.

d (cm)	( $N_{coinc} \pm \sigma_{N_{coinc}}$ )	$\epsilon \pm \sigma_\epsilon$
13	7000 $\pm$ 80	0.001 34 $\pm$ 0.00002
18	4530 $\pm$ 70	0.000 70 $\pm$ 0.00001
23	2450 $\pm$ 50	0.000 47 $\pm$ 0.00001
28	3730 $\pm$ 60	0.000 295 $\pm$ 0.000006
38	3200 $\pm$ 60	0.000 177 $\pm$ 0.000004
48	2790 $\pm$ 50	0.000 115 $\pm$ 0.000003

Table 21 Efficiency  $\epsilon$  values from the coincidences of the two gamma rays of 511 keV for CeBr<sub>3</sub> detectors.

### C. Efficiency from Co coincidences

The efficiencies of the two <sup>60</sup>Co peaks can be calculated using another method that exploits the coincidences. In fact, the lifetimes of the states for the transitions from the 2<sup>nd</sup> to the 1<sup>st</sup> excited state ( $t_{1/2}=0,59$  ps) and from the 1<sup>st</sup> excited to the ground state ( $t_{1/2}=0,735$  ps) are smaller than the time resolution of the detectors and so the two gamma rays of 1173 and 1333 keV can be considered emitted in coincidence.

When the detector ch0 acquires an event corresponding to a 1173 keV gamma, it is known that a <sup>60</sup>Co decay took place and also a 1333 keV gamma was emitted. Knowing the counts in the 1173 keV peak of ch0 and the 1333 keV gamma acquired in coincidence by detector ch1 it is possible to calculate the efficiency of detector ch1 to detect

1333 keV gammas through the formula

$$\epsilon = \frac{N_{1333,coinc,ch1}}{N_{1173,ch0} \cdot W(\pi)}$$

where  $N_{1173,ch0}$  is the number of counts of the 1173 keV peak acquired by detector ch0,  $N_{1333,coinc,ch1}$  is the number of 1333 keV gamma acquired by detector ch1 in coincidence with the 1173 keV gamma acquired by detector ch0,  $W(\pi)$  is the  $^{60}\text{Co}$  angular distribution for the detectors positioned at an angle of  $\pi$ . To decide the maximum time interval between two events considered coincident, we proceeded in the following way: we gated the data imposing the conditions on the energies (the belonging to the 1173 keV peak and the 1333 keV peak respectively), then made a histogram of the time differences  $\Delta t = |t_{ch0} - t_{ch1}|$  of events recorded by both detectors within an interval of  $1 \cdot 10^6$  ps. An example of such histogram is displayed in Figure 24. From this time distribution we were able to identify the time interval in which the coincidences distribute. The data time gating was set to an interval of  $3 \cdot 10^4$  ps for coincident events. The values obtained for the peak counts and the corresponding coincidences are reported in Table 22. Since the decay of  $^{60}\text{Co}$  is not isotropic, in the calculation of the efficiency it was necessary to introduce a correction due to the angular correlation of the two emitted gamma rays. The  $^{60}\text{Co}$  angular distribution is well known and can be written as

$$W(\theta) = 1 + \frac{1}{8} \cos^2 \theta + \frac{1}{24} \cos^4 \theta$$

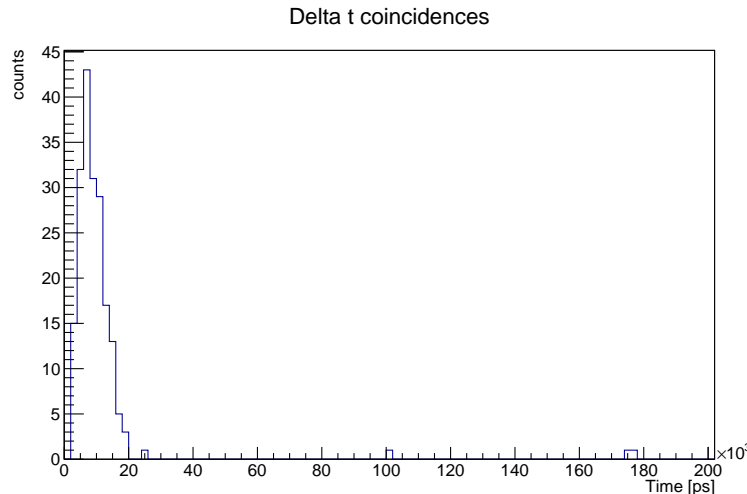


Figure 24  $\Delta t = |t_{ch0} - t_{ch1}|$  obtained considering 1333 keV gamma acquired by the detector and 1173 keV gamma acquired by detector ch1 within a time interval of  $1 \cdot 10^6$  ps.

Applying the same reasoning to the other gamma and inverting the detectors ch0 and ch1 in the previous formula, it is possible to obtain also the other efficiencies. One of the advantages of this method is that it is independent of the information on the source activity. The obtained values are reported in Table 23. We chose to apply this method to just one acquisition (the run acquired with the  $\text{LaBr}_3(\text{Ce})$  detectors placed both at 13 cm from the source that has an higher statistics) and then compared the results obtained with the one calculated in Subsection II.9.A to see if they are consistent. The compatibility  $\lambda$  between the efficiencies calculated using the two methods is reported in Table 24 and is good or very good in all the four cases.

channel	1173 keV	1333 keV	&1173 keV	&1333 keV
ch <sub>0</sub>	$23700 \pm 200$	$20\,700 \pm 100$	$210 \pm 10$	$190 \pm 10$
ch <sub>1</sub>	$23300 \pm 200$	$21\,000 \pm 100$	$190 \pm 10$	$210 \pm 10$

Table 22 The values labeled 1173 keV and 1333 keV are the counts under the respective acquired by the detectors. The values labeled &1173 keV are the number of 1173 keV gamma the detector acquired in coincidence with the 1333 keV gamma in the other detector. The values labeled &1333 keV are the number of 1333 keV gamma the detector acquired in coincidence with the 1173 keV gamma in the other detector.

channel	$\epsilon_{1173}$	$\epsilon_{1333}$
<i>ch<sub>0</sub></i>	$0.0084 \pm 0.0005$	$0.0070 \pm 0.0004$
<i>ch<sub>1</sub></i>	$0.0078 \pm 0.0005$	$0.0074 \pm 0.0004$

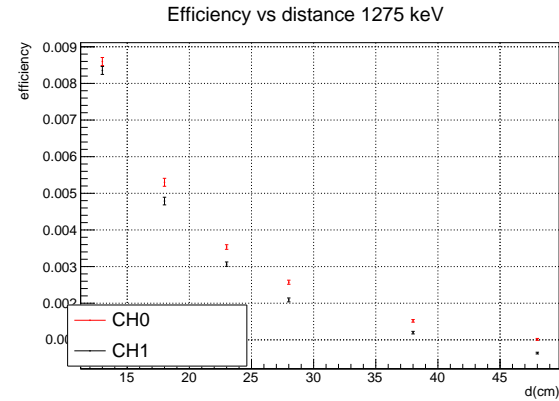
Table 23 Efficiencies of the  $^{60}\text{Co}$  peaks calculated for the  $\text{LaBr}_3(\text{Ce})$  detectors positioned at 13 cm from the source.

channel	$\lambda_{1173}$	$\lambda_{1333}$
<i>ch<sub>0</sub></i>	0.6	1.3
<i>ch<sub>1</sub></i>	0.6	1.5

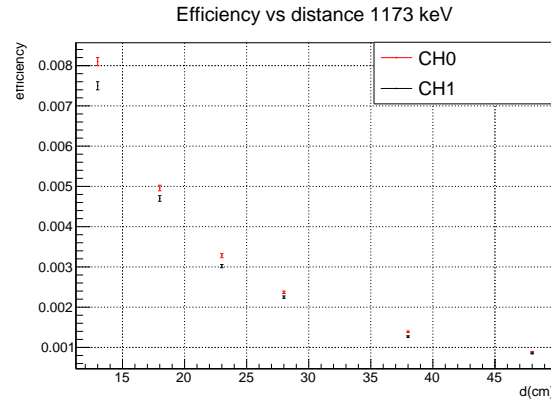
Table 24 Compatibility of the efficiencies calculated as described in Subsection II.9.A and the ones obtained with the coincidence method.

## 10. Efficiency vs distance and Efficiency vs energy

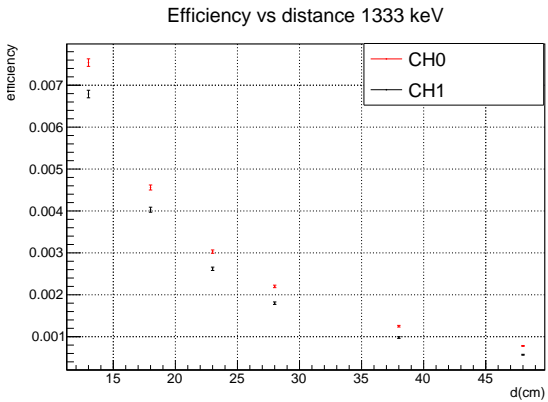
In this part we collect the results obtained for the efficiency of the four full energy peaks. Figure 25 shows the efficiency for the four full energy peaks as a function of the distance for the two  $\text{LaBr}_3(\text{Ce})$  detectors; the efficiencies are obtained calculating the integral of the full energy peaks (method A). Similarly, Figure 26 shows the efficiency for the four full energy peaks as a function of the distance for the two  $\text{CeBr}_3$  detectors; the efficiencies are obtained calculating the integral of the full energy peaks (method A). Instead, in Figure 27 we report the efficiencies for the 511 keV gamma as a function of the distance; the efficiencies are calculated using the coincidences (method B).



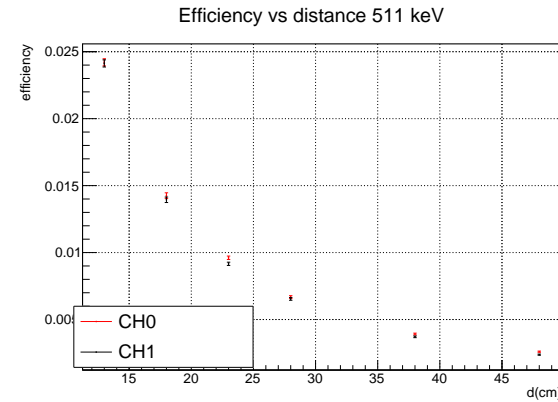
(a) Efficiency vs distance for the 1275 keV peak in  $\text{LaBr}_3(\text{Ce})$  detectors



(b) Efficiency vs distance for the 1173 keV peak in  $\text{LaBr}_3(\text{Ce})$  detectors



(c) Efficiency vs distance for the 1333 keV peak in  $\text{LaBr}_3(\text{Ce})$  detectors



(d) Efficiency vs distance for the 511 keV peak in  $\text{LaBr}_3(\text{Ce})$  detectors

Figure 25 In 25a, 25b, 25d and 25c the efficiency of the 1275, 1173, 1333 and 511 keV peaks vs distance for the  $\text{LaBr}_3(\text{Ce})$  detectors. The red dots refer to detector ch0 and the blue dots to detector ch1.

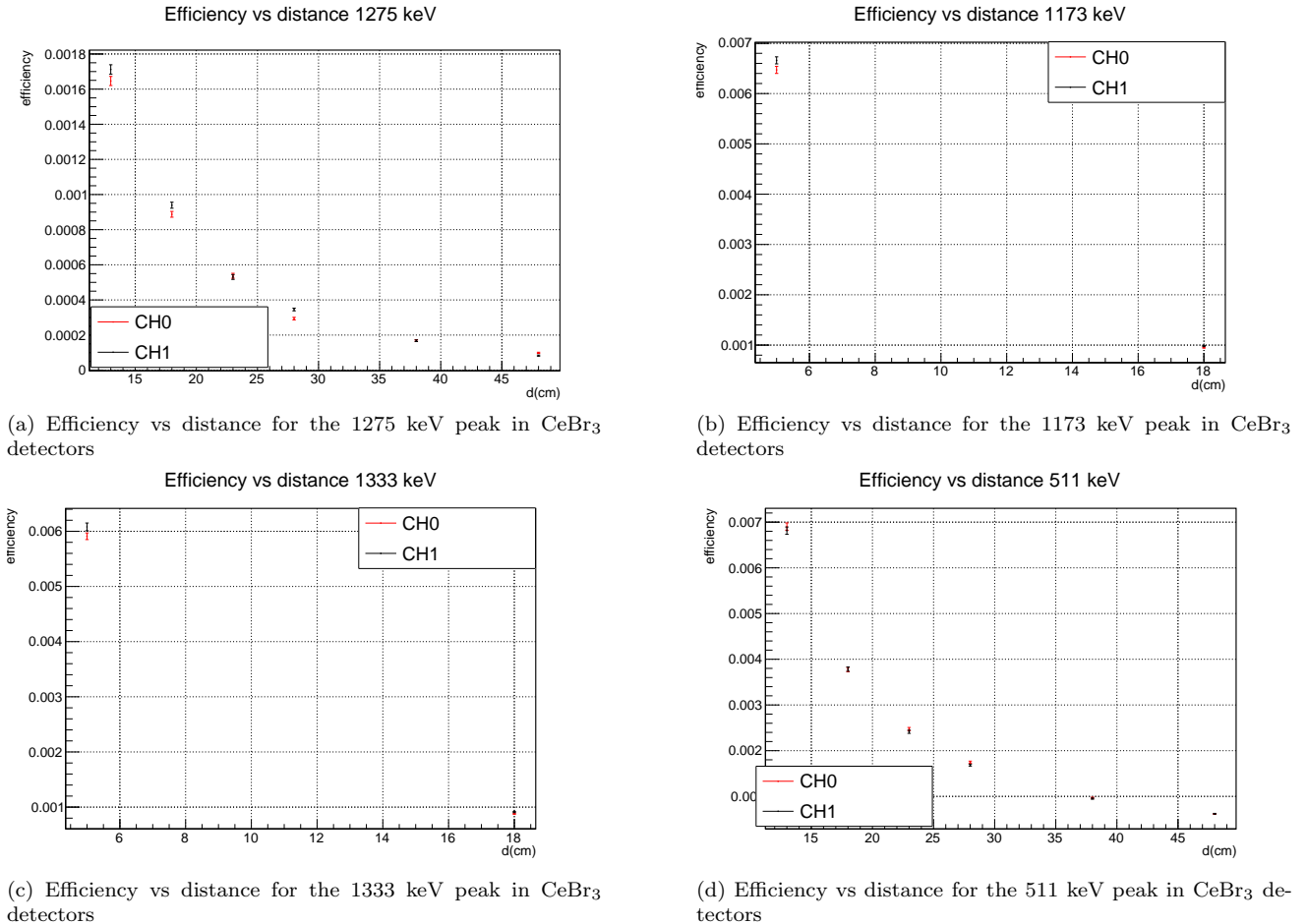


Figure 26 In 26a, 26b, 26c and 26d the efficiency of the 1275, 1173, 1333 and 511 keV peaks vs distance for the CeBr<sub>3</sub> detectors. The red dots refer to detector ch0 and the blue dots to detector ch1.

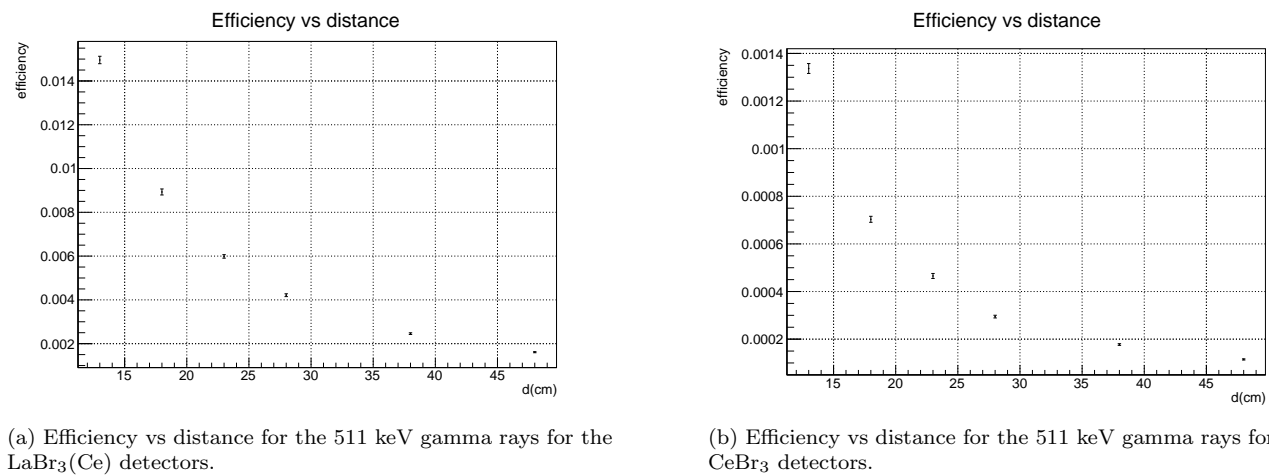
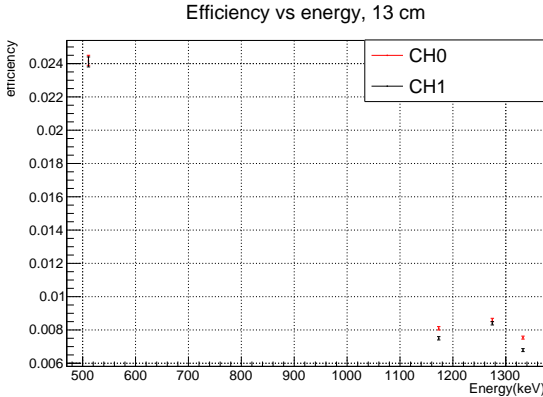


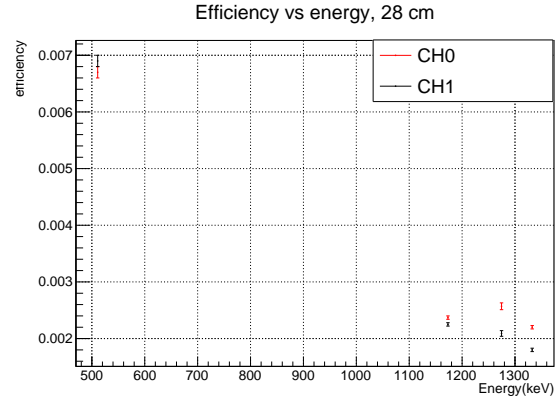
Figure 27 In 27a and in 27b, the efficiency from the coincidences of the two 511 keV gamma rays vs distance for the LaBr<sub>3</sub>(Ce) and CeBr<sub>3</sub> detectors respectively.

Figure 28 shows the efficiency as a function of the energy for the LaBr<sub>3</sub>(Ce) detectors placed at 13 cm (28a) and 18 cm (28b) from the source. The efficiencies used for the 511 keV peak are the ones obtained using the net counts under the peak (method A). Figure 29 shows the efficiency as a function of the energy for the CeBr<sub>3</sub> detectors placed

at 18 cm from the source. The efficiency is expected to decrease with the energy. From our data the efficiency seems to have an irregular trend: the 1173 keV peak has an efficiency lower than the 1275 keV peak. Probably, this is due to the fact that in the analysis we did not consider the summing out effects. It is possible to take them into account, for example, using simulations. However this is beyond the scope of this experience. For this reason, we decided not to proceed to a fitting of the efficiency values.



(a) Efficiency vs energy; both  $\text{LaBr}_3(\text{Ce})$  detectors placed at 13 cm from the source



(b) Efficiency vs energy; both  $\text{LaBr}_3(\text{Ce})$  detectors placed at 28 cm from the source

Figure 28 Efficiency of the 511, 1275, 1173 and 1333 keV peaks as a function of the energy for the  $\text{LaBr}_3(\text{Ce})$  detectors both placed at 13 cm (28a) and 28 cm (28b) from the source.

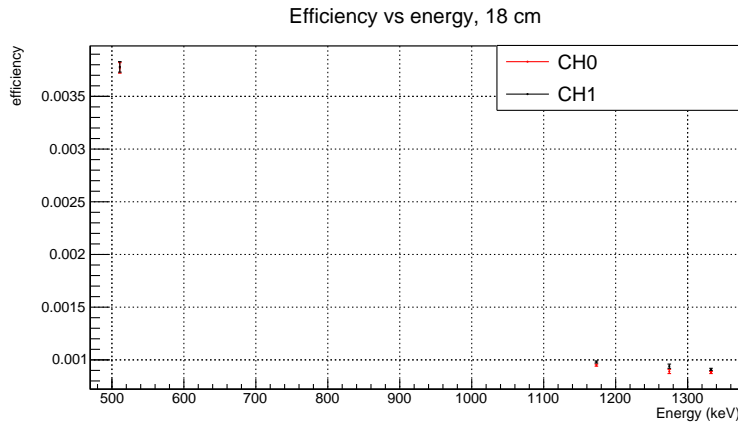


Figure 29 Efficiency of the 511, 1275, 1173 and 1333 keV peaks as a function of the energy for the  $\text{CeBr}_3$  detectors placed at 18 cm.

## 11. Speed of light

The measurement of the speed of light requires to maximally optimize the time characteristics of the set up. For this reason, we used the  $\text{CeBr}_3$  detectors, which have a faster time response, and we changed the setting of the acquisition system, swapping from PHA to PSD mode. During this part of the experiment only the  $^{22}\text{Na}$  source was used. We acquired the spectra placing the detectors in the two configurations displayed in Figure 30

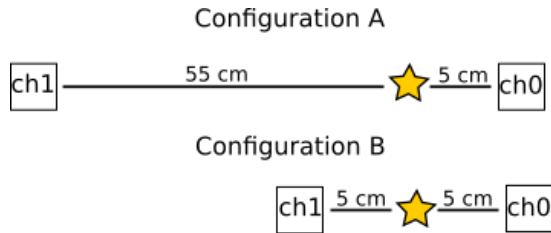


Figure 30 Scheme of the two configurations A and B we used to measure the speed of light. The star indicates the source's position.

In the configuration A the detector ch0 was placed at 5 cm from the source and the detector ch1 was placed at 55 cm from the source; in the configuration B both detectors were placed at 5 cm from the source. In both the configurations, the two detectors were connected to cables of different lengths; the longest, which acted as a delay cable, was connected to detector ch0.

With the adopted setup, several systematic errors come into play; here we list the principal contributions:

- The source is mounted manually on a plastic support: it may not be perfectly centered.
- The detectors are placed on a plane surface but they may not be at the exact same height and not be perfectly parallel.
- The detectors may not be placed at the same exact distance: the position was fixed using a measuring tape with cm intervals. In addition, since a specific holder for these detectors was not available and the detectors had cylindrical shapes, they may have slightly moved or rotated while being fixed in position.
- The measured process is the annihilation of a  $e^+$  (originated in the  $\beta^+$  decay) with an  $e^-$ , which generates 2 coincident  $\gamma$ -rays. The annihilation process does not necessarily take place in the source spot, but may happen within a certain distance.

Of all the above contributions, the dominant one is the positioning of the detectors: in fact, we estimated the error in positioning the detectors to be 2 mm. After assessing the different contributions to the error on distance, it is possible to extract a measurement of the velocity of light through the formula

$$c = \frac{\Delta s}{\Delta t_B - \Delta t_A}$$

where

- $\Delta s=50$  cm is the difference in space between the two configurations.
- $\Delta t_A$  and  $\Delta t_B$  are the difference in time between the arrival time of the 511 keV gamma to the detector ch0 and the arrival time to the detector ch1. In Figure 31 the time distribution of the differences of arrival time between detector ch0 and ch1 are displayed. These time distributions are obtained imposing that the events of interest lay under the 511 keV peak and that the time difference between event in ch0 and in ch1 is not larger than  $1 \cdot 10^6$  ps. The values for  $\Delta t_A$  and  $\Delta t_B$  are obtained performing Gaussian fits over these two distributions:  $\Delta t_A = 6244 \pm 4$  ps and  $\Delta t_B = 7904 \pm 6$  ps.

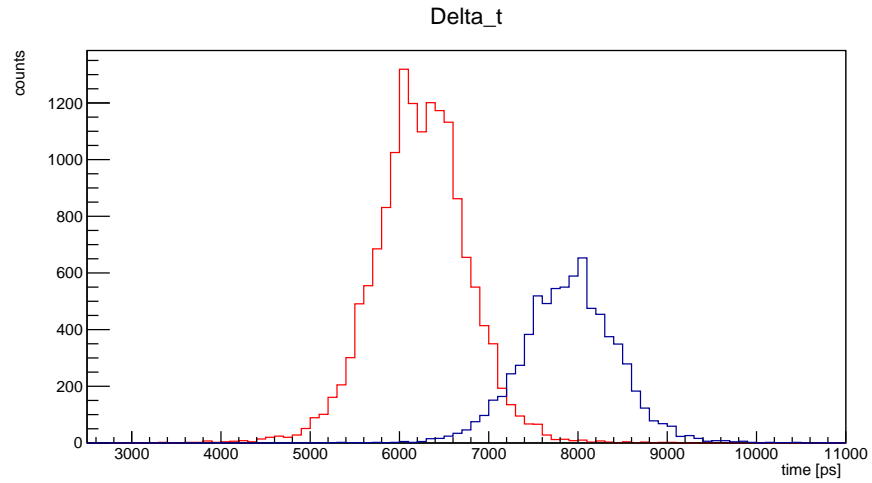


Figure 31  $\Delta t_A$  and  $\Delta t_B$  time distributions; the red histogram refers to the configuration A, while the blue one to the configuration B.

Eventually, our measurement of the speed of light was

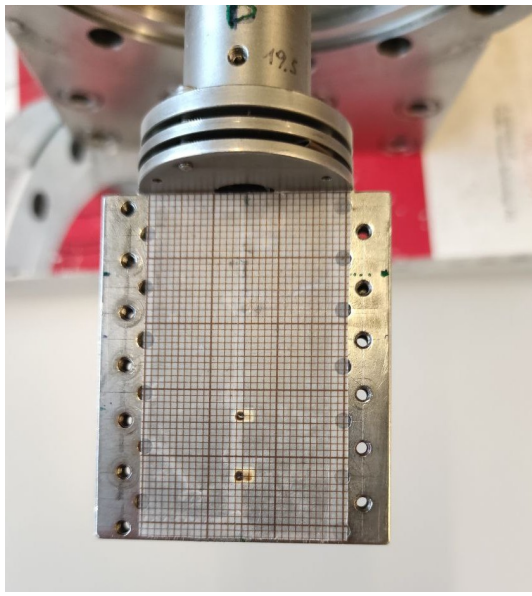
$$c = 3.012 \pm 0.001 \cdot 10^8 \text{ m/s}$$

### III. II PART: CALIBRATION OF THE AN2000 ACCELERATOR

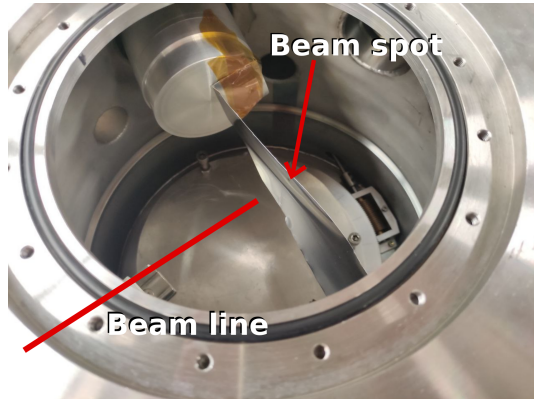
In this part we report the energy calibration of the AN2000 accelerator installed at the Laboratori Nazionali di Legnaro. This accelerator is used to perform measurements of ion beam analysis and it is important to know exactly the energy of the accelerated particles. A technique to calibrate the accelerator is to produce well known resonances reactions: since resonances reactions occur at specific energies, it is possible to exploit the correspondence between the measured parameters of the resonance and the accelerator settings.

#### 1. Experimental set up

The experimental set up comprised the accelerator AN2000, a scattering chamber, an Aluminium target and two detectors: a germanium detector and a LaBr<sub>3</sub>(Ce) scintillator. The AN2000 electrostatic accelerator can accelerate both protons and helium; in this experiment it provided a proton beam at energies below 2 MeV. The beam energy can be varied modifying the magnetic field of the magnets that bend and select the accelerated particles. The values of the magnetic field are read by a nmr probe and a gaussmeter. In order to know a rough correspondence between the nmr probe values and the energy of the accelerated protons, we used a calibration table provided by the LNL. It is possible to monitor the beam current using an ORTEC current integrator and the integrated charge provided by the beam is given by an ORTEC dual counter. The protons accelerated were sent to the target, placed inside the scattering chamber. The target was an Aluminium foil with 0.10 mm thickness and 99 % purity. To check the impact point of the beam inside the chamber, we made a test using a piece of graph paper mounted on an holder. By checking the position of the beam spot on the paper, it was possible to position correctly the Aluminium inside the chamber. Figure 32 shows the irradiated graph paper and the Aluminium target inside the scattering chamber. After putting the Aluminium target in place, the chamber was put into vacuum. In this procedure a combination of



(a) Beam spots on graph paper



(b) Aluminium target in place, photo taken after the irradiation

Figure 32 32a shows the beam spots on the graph paper. In 32b it is possible to see the position of the Aluminium target inside the chamber; also in this case the beam spot is visible.

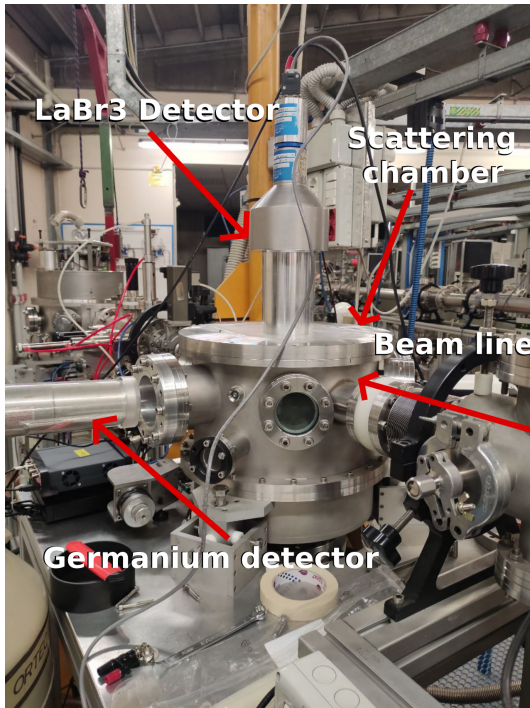
primary (scroll pump) and secondary (turbomolecular pump) stage pumps was used. The vacuum inside the chamber was set to  $10^{-6} - 10^{-7}$  mBar.

In this configuration we studied three resonances [6], produced by the two reactions  $^{27}\text{Al}(\text{p},\gamma)^{28}\text{Si}$  and  $^{27}\text{Al}(\text{p},\text{p}'\gamma)^{27}\text{Al}$ :

- $^{27}\text{Al}(\text{p},\gamma)^{28}\text{Si}$ : a resonant reaction can be produced with a proton beam of  $991.86 \pm 0.03$  keV in the laboratory frame; in the reaction a gamma ray of energy  $E_\gamma = 1779$  keV is produced. The width of the resonance is  $\Gamma_{CM} = 0.070 \pm 0.014$  keV.
- $^{27}\text{Al}(\text{p},\text{p}'\gamma)^{27}\text{Al}$ : a resonant reaction can be produced with a proton beam of  $1664.4 \pm 0.2$  keV or  $1683.57 \pm 0.13$  keV;

in both reactions a gamma ray of energy  $E_\gamma = 843$  keV is produced. The width of the resonance in the first case is  $\Gamma_{CM} = 0.45 \pm 0.05$  keV; in the second case it is  $\Gamma_{CM} < 0.2$  keV.

In order to study these reactions, we acquired the characteristic gamma rays emitted by the populated resonant states. To this scope we used two different detectors: the  $\text{LaBr}_3(\text{Ce})$  has a lower energy resolution, but it was possible to mount it directly on top of the scattering chamber; on the other hand, the Germanium detector provided a higher energy resolution, but since it has to be cooled down to the temperature of liquid nitrogen, it was placed more distant from the scattering point in order to allow space for the dewar containing liquid nitrogen. This affected the efficiency of the detector and it turned out that it was able to acquire the desired signal only in the more intense  $^{27}\text{Al}(\text{p},\text{p}'\gamma)^{27}\text{Al}$  reaction. Both detectors were connected to the CAEN digitizer and the acquisition was done using the CoMPASS software in PHA mode. Figure 33 shows the scattering chamber and the two detectors in place.



(a) Experimental set up: scattering chamber and detectors



(b) Detail of the germanium detector: the dewar does not allow to place it closer to the scattering chamber

Figure 33 33a shows the adopted experimental set up; 33b shows the distance between the Germanium detector and the scattering chamber.

## 2. Resonant reactions and Yield

In a nuclear reaction, the cross section is strongly modified in the presence of resonance. In fact, at the energy of the resonance the cross section is highly enhanced and its behavior, in a first approximation, can be described by a Breit-Wigner function. The upper part of Figure 34 shows the cross section for a resonance placed at 500 keV. In the experiment we performed a resonance scan: we varied in small steps the energy of the incoming particle and acquired the corresponding gamma spectrum. Instead of analyzing the data calculating the cross section, we calculated another physical quantity, the yield, which is defined as

$$Y = \frac{\text{number of nuclear reactions}}{\text{number of incident beam particles}}$$

Using the quantities we measured in the laboratory, we obtained

$$Y = \frac{N_{peak}}{N_{counter}}$$

where  $N_{peak}$  is the number of counts under the full energy peak of the gamma emitted in the resonant reaction and  $N_{counter}$  are the number of counts registered by the counter during the acquisition. The yield is connected to the cross section and it is possible to extract information on the resonance. The yield curve, as it is possible to see from the lower part of Figure 34, has different shapes depending on the target thickness. We worked in the infinite target approximation (the incident particle is stopped inside the target):

- the yield curve has a flat behavior for an energy lower than the resonance
- approaching the resonance energy the yield curve starts increasing
- the inflection point of the yield curve correspond to the energy of the resonance
- after the inflection point the yield curves increases and reaches another flat region
- the energy region comprised between the 25% and the 75% of the rise of the yield curve correspond to the resonance width

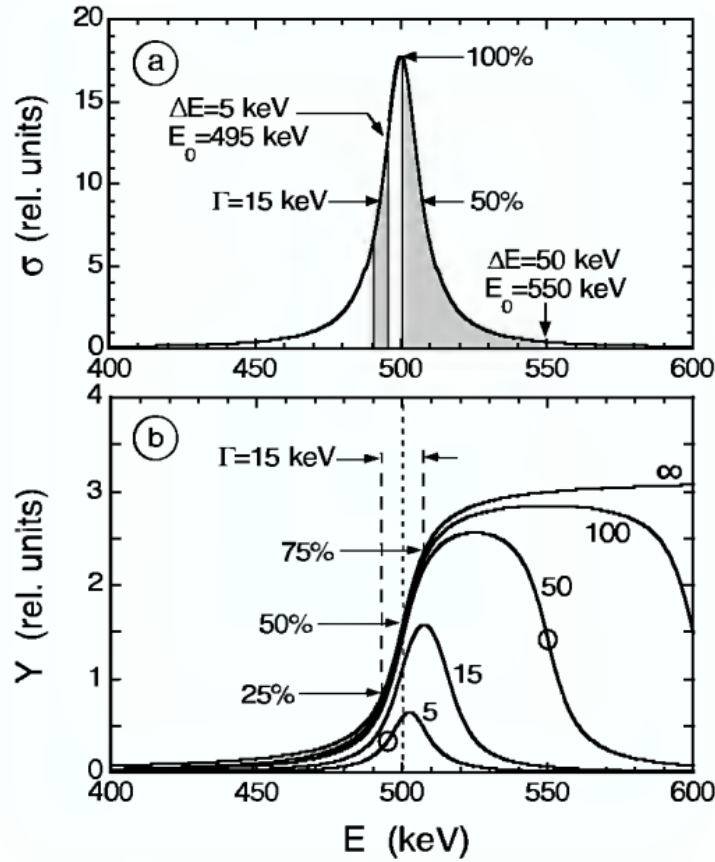


Figure 34 The upper part of the Figure shows the cross section of a Breit-Wigner resonance located at 500 keV and width  $\Gamma=15$  keV. The lower part shows the yield curve; the yield depends on the bombarding energy and the target thickness. The yield curve for the infinite thickness approximation is the one labeled as  $\infty$ . Picture taken from [7].

### 3. Data acquisition

To perform the resonance scan we proceeded in the following way:

- We set the accelerator parameters so that the correspondence nmr probe values - energy of the proton was close to the one required by the resonant reactions. In this operation we modified the nmr values according to the tables provided in the laboratory.

- We started acquiring different runs changing slightly the nmr values, proceeding in steps of the order of few keV.
- Performing a rough online analysis using the CoMPASS software we were able to identify the nmr values corresponding to the resonant behavior. We scanned region with smaller energy steps.

The data acquisition took place on three consecutive days, on November 23,24 and 25. The measurement was divided in the following steps:

- November 23: we mounted the set up and acquired a spectrum with a  $^{60}\text{Co}$  and a  $^{137}\text{Cs}$  source in place in order to calibrate the detectors in energy.  
We acquired the first data set for the scan of the 992 keV resonance.
- November 24: we acquired a data set for scan of the 992 keV resonance and a data set for the scan of the 1664 and 1685 keV resonances.
- November 25: we acquired a data set for scan of the 992 keV resonance and a data set for the scan of the 1664 and 1685 keV resonances.
- During the nights we acquired long background runs for the  $\text{LaBr}_3(\text{Ce})$  detector.

In the following, we analysed separately the data acquired on different days.

#### 4. Adopted notation on the errors

In this part of the report for improving the readability we adopted the following conventions:

- The energies of the resonances in the following are labeled just as 992 keV, 1664 keV and 1684 keV. Altough the error is not indicated, it is taken into account in the analysis.
- The error of the NMR measurements has been estimated as  $\frac{ptl}{\sqrt{12}}$ , where the ptl value was set as the third digit starting from the right ( $\sigma_{NMR}=0.000003 \cdot 10^4 \text{Gauss}$ ).
- The error on the Gaussmeter was taken as  $\frac{ptl}{\sqrt{12}}$ , where the ptl is the last digit ( $\sigma_{Gauss}=0.0003 \text{ kGauss}$ ).
- The error on the counter value is assumed to be negligible compared to the one of the other measurements.

## 5. Data analysis

### A. Energy calibration of the detectors

As we already explained in Subsection [II.3](#), we firstly proceeded to calibrate in energy both the germanium and the LaBr<sub>3</sub>(Ce) detectors. In this case we used a <sup>137</sup>Cs source and a <sup>60</sup>Co source. As before, we performed a linear calibration and we report in Table [25](#) the mean values  $N_{channel}$  and in Table [26](#) the calibration parameters. The linear fits are shown in Figure [35](#). Again, we proceeded to check the linear correlation through the  $\rho$ -t test. From the parameters reported in Table [27](#) (the name of the parameters are the same as in the aforementioned section) it is possible to affirm that the hypothesis of not linear correlation is false with 99% confidence level for both the linear fits performed to calibrate the detectors.

channel	$E_\gamma$ [keV]	$N_{channel_{LaBr}}$ [ch]
<i>Germanium</i>	612	2582.4 $\pm$ 0.2
	1173	4581.9 $\pm$ 0.3
	1333	5206.0 $\pm$ 0.3
<i>LaBr<sub>3</sub>(Ce)</i>	612	737.34 $\pm$ 0.04
	1173	1311.1 $\pm$ 0.1
	1333	1491.8 $\pm$ 0.1

Table [25](#) Values of the mean obtained from the Gaussian fit of the full energy peaks of <sup>137</sup>Cs and <sup>60</sup>Co decays.

channel	$m$ [keV/ch]	$q$ [keV]
<i>Germanium</i>	0.255 75 $\pm$ 0.00004	1.2 $\pm$ 0.1
<i>LaBr<sub>3</sub>(Ce)</i>	0.8901 $\pm$ 0.0001	5.4 $\pm$ 0.1

Table [26](#) Values of the calibration parameters of the Germanium and the LaBr<sub>3</sub>(Ce) detectors.

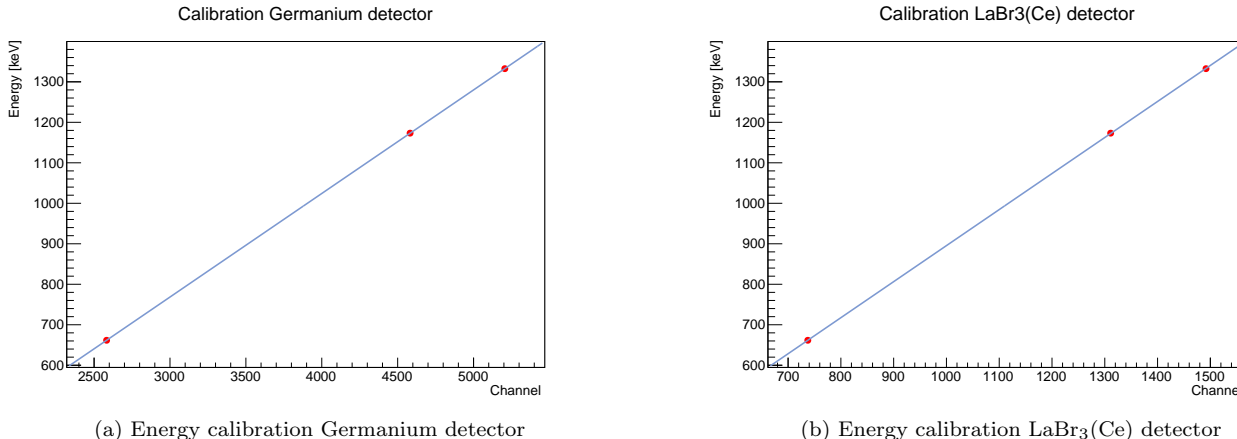


Figure [35a](#) In [35a](#) it is shown the energy calibration for the Germanium detector, while in [35b](#) it is displayed the energy calibration for the ch0 LaBr<sub>3</sub>(Ce) detector.

channel	$\rho$	$N$	$t$	%
<i>Germanium</i>	0.9999999	3	2236	99%
<i>LaBr<sub>3</sub>(Ce)</i>	0.999998	3	500	99%

Table [27](#) Parameters obtained with the t-student test; as above the subscripts refer to the two different types of detectors used: LaBr<sub>3</sub>(Ce) and Germanium.

### B. Background subtraction for LaBr<sub>3</sub>(Ce) detector

For the measures obtained with the LaBr<sub>3</sub>(Ce) detector we decided to take a run of the background to be subtracted to the energy spectrum of each acquisition before evaluating the number of counts under the peaks at 1779 and 843 keV. In Fig. 36a and 36b we reported the background superimposed to the energy spectrum for the total spectrum and under the 1779 keV peak.

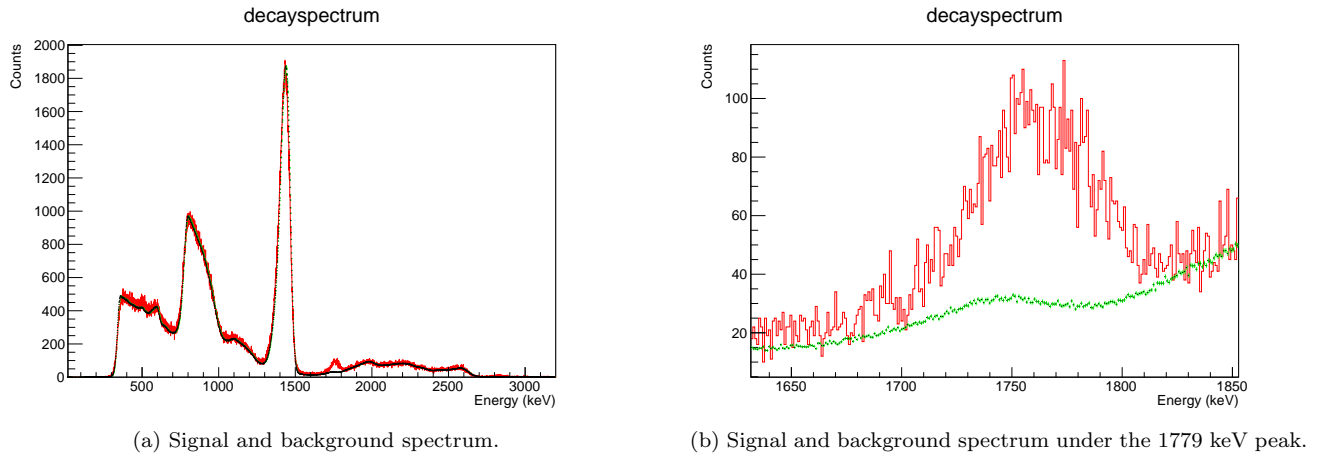


Figure 36

### C. Background subtraction for Germanium detector

The Germanium detector has a lower intrinsic background respect to the LaBr<sub>3</sub>(Ce) detector and so we used a different method for determining the background contribution. Using the Germanium detector, we acquired data only for the resonances at 1664 keV and 1684 keV and the signals of interest are the net counts under the 843 keV peak. Since there are no other peaks in the energy region near 843 keV, we calculated the net area as

$$A = \sum_{i=L}^U C_i - n \left( \sum_{i=L-m}^{L-1} C_i + \sum_{i=U+1}^{U+m} C_i \right) / 2m$$

where  $C_i$  are the counts in the  $i$ -th bin, L is the lower limit of the region of interest of the peak, U is the upper limit of the region of interest of the peak, n is the number of bins under the peak and m the number of bins on which the background contribution is evaluated. Figure 37 shows graphically this notation; in our calculation we used m=n.

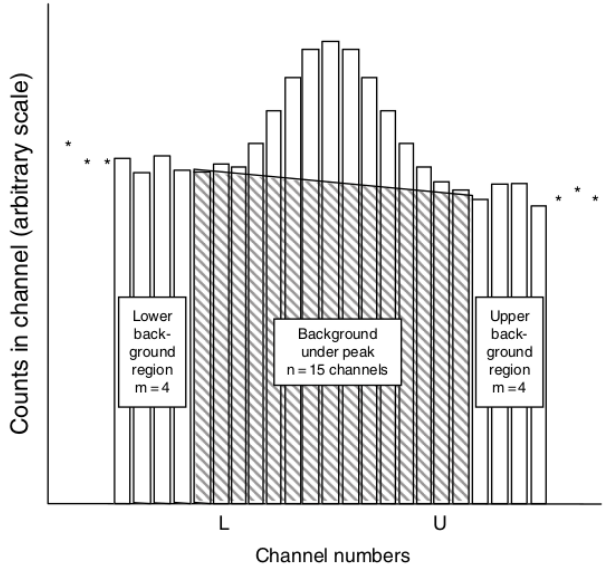


Figure 37 Background subtraction method used for the Germanium detector. Picture taken from [1]

#### D. Resonances at 992 keV with LaBr<sub>3</sub>(Ce) detector, data collected on November 23, 24 and 25, 2022

In the following we reported the nmr and gaussmeter values with the corresponding net counts under the peak and the calculated yield for the transition at 1779 keV for the 992 keV resonance acquired on November 23, 24 and 25 using the LaBr<sub>3</sub>(Ce) detector (Table 28, 29, and 30).

nmr (10 kGauss)	Gaussmeter (kGaus)	net counts	Yield
0.161837	1.610	3590 ±60	0.00438 ±0.00007
0.162406	1.616	3930 ±60	0.00428 ±0.00007
0.162601	1.618	3510 ±60	0.00411 ±0.00007
0.162803	1.620	3540 ±60	0.00555 ±0.00009
0.163006	1.622	6410 ±80	0.0095 ±0.0001
0.163206	1.624	11 500 ±100	0.00963 ±0.00009
0.163407	1.626	12 300 ±100	0.00950 ±0.00009
0.163607	1.628	12 200 ±100	0.00962 ±0.00009
0.163809	1.630	15 800 ±100	0.00969 ±0.00008
0.164040	1.632	13 400 ±100	0.00988 ±0.00009
0.164400	1.636	13 300 ±100	0.01005 ±0.00009
0.164727	1.639	30 500 ±200	0.00958 ±0.00005

Table 28 Number of net counts of the full energy peak at 1779 keV as a function of the nmr and calculated Yield. Data acquired on November 23.

<b>nmr (10 kGauss)</b>	<b>Gaussmeter (kGaus)</b>	<b>net counts</b>	<b>Yield</b>
0.161805	1.610	6650 ±80	0.00479 ±0.00006
0.162501	1.617	5970 ±80	0.00477 ±0.00006
0.162550	1.618	4820 ±70	0.00475 ±0.00007
0.162599	1.618	5240 ±70	0.00474 ±0.00007
0.162648	1.619	5290 ±70	0.00463 ±0.00006
0.162713	1.619	3220 ±60	0.00467 ±0.00008
0.162746	1.620	5140 ±70	0.00466 ±0.00006
0.162795	1.620	2610 ±50	0.00458 ±0.00009
0.162860	1.621	4130 ±60	0.00454 ±0.00007
0.162910	1.621	3060 ±60	0.00474 ±0.00009
0.162959	1.622	3320 ±60	0.00483 ±0.00008
0.163058	1.623	2910 ±50	0.0053 ±0.0001
0.163157	1.624	3120 ±60	0.0079 ±0.0001
0.163211	1.624	7890 ±90	0.0091 ±0.0001
0.163258	1.625	7690 ±90	0.0093 ±0.0001
0.163308	1.625	5990 ±80	0.0092 ±0.0001
0.163358	1.626	7630 ±90	0.0097 ±0.0001
0.163409	1.626	7080 ±80	0.0095 ±0.0001
0.163460	1.627	3890 ±60	0.0097 ±0.0002
0.163495	1.627	6600 ±80	0.0095 ±0.0001
0.163560	1.628	3790 ±60	0.0095 ±0.0002
0.163611	1.628	3510 ±60	0.0098 ±0.0002
0.163660	1.629	5670 ±80	0.0095 ±0.0001
0.163711	1.629	3360 ±60	0.0097 ±0.0002
0.163913	1.631	6090 ±80	0.0096 ±0.0001

Table 29 Number of net counts of the full energy peak at 1779 keV as a function of the nmr and calculated Yield. Data acquired on November 24.

<b>nmr (10 kGauss)</b>	<b>Gaussmeter (kGaus)</b>	<b>net counts</b>	<b>Yield</b>
0.161652	1.609	2500 ±50	0.0049 ±0.0001
0.162304	1.615	8840 ±90	0.00472 ±0.00005
0.162718	1.619	1660 ±40	0.0045 ±0.0001
0.162812	1.620	1820 ±40	0.0051 ±0.0001
0.162845	1.621	1840 ±40	0.0057 ±0.0001
0.162910	1.621	2800 ±50	0.0078 ±0.0001
0.162942	1.622	2630 ±50	0.0080 ±0.0002
0.163015	1.622	3390 ±60	0.0094 ±0.0002
0.163102	1.623	3600 ±60	0.0099 ±0.0002
0.163103	1.623	4610 ±70	0.0098 ±0.0001
0.163512	1.627	3270 ±60	0.0101 ±0.0002
0.163998	1.632	3370 ±60	0.0100 ±0.0002

Table 30 Number of net counts of the full energy peak at 1779 keV as a function of the nmr and calculated Yield. Data acquired on November 25.

#### E. Resonances at 1664 and 1684 keV with LaBr<sub>3</sub>(Ce) and Germanium detectors, data collected on November 24 and 25, 2022

In the following we report the nmr and gaussmeter values with the corresponding net counts under the peak and the calculated yield for the transition at 843 keV for the 1664 and 1684 keV resonances acquired on November 24 and 25 using the LaBr<sub>3</sub>(Ce) and the Germanium detectors (Table 31, 32, 33 and 34).

<b>nmr (10 kGauss)</b>	<b>Gaussmeter (kGaus)</b>	<b>net counts</b>	<b>Yield</b>
0.209941	2.090	196 800 $\pm$ 400	0.03713 $\pm$ 0.00008
0.210096	2.091	72 400 $\pm$ 300	0.0373 $\pm$ 0.0001
0.210405	2.094	74 200 $\pm$ 300	0.0453 $\pm$ 0.0002
0.210701	2.097	74 200 $\pm$ 300	0.0456 $\pm$ 0.0002
0.210796	2.190	58 600 $\pm$ 200	0.0463 $\pm$ 0.0002
0.210998	2.100	63 300 $\pm$ 300	0.0661 $\pm$ 0.0003
0.211104	2.102	95 600 $\pm$ 300	0.0682 $\pm$ 0.0002
0.211309	2.103	83 800 $\pm$ 300	0.0696 $\pm$ 0.0002
0.211547	2.106	87 100 $\pm$ 300	0.0687 $\pm$ 0.0002
0.211900	2.109	99 100 $\pm$ 300	0.0707 $\pm$ 0.0002
0.212106	2.111	104 200 $\pm$ 300	0.0946 $\pm$ 0.0003
0.212301	2.113	134 800 $\pm$ 400	0.1205 $\pm$ 0.0003
0.212511	2.115	160 000 $\pm$ 400	0.1219 $\pm$ 0.0003
0.213104	2.121	138 500 $\pm$ 400	0.1251 $\pm$ 0.0003
0.213699	2.127	106 600 $\pm$ 300	0.1278 $\pm$ 0.0004

Table 31 Number of net counts of the full energy peak at 843 keV as a function of the nmr and calculated Yield using the LaBr<sub>3</sub>(Ce) detector. Data acquired on November 24.

<b>nmr (10 kGauss)</b>	<b>Gaussmeter (kGaus)</b>	<b>net counts</b>	<b>Yield</b>
0.210403	2.094	129 000 $\pm$ 400	0.0444 $\pm$ 0.0001
0.210704	2.097	49 300 $\pm$ 200	0.0540 $\pm$ 0.0002
0.210752	2.090	113 100 $\pm$ 300	0.0618 $\pm$ 0.0002
0.210792	2.098	91 700 $\pm$ 300	0.0676 $\pm$ 0.0002
0.210798	2.098	90 200 $\pm$ 300	0.0678 $\pm$ 0.0002
0.210896	2.099	92 500 $\pm$ 300	0.0721 $\pm$ 0.0002
0.211708	2.107	116 600 $\pm$ 300	0.0842 $\pm$ 0.0002
0.211895	2.109	139 600 $\pm$ 400	0.0835 $\pm$ 0.0002
0.212012	2.110	152 200 $\pm$ 400	0.1241 $\pm$ 0.0003
0.212107	2.111	117 200 $\pm$ 300	0.1277 $\pm$ 0.0004
0.212212	2.112	149 800 $\pm$ 400	0.1289 $\pm$ 0.0003

Table 32 Number of net counts of the full energy peak at 843 keV as a function of the nmr and calculated Yield using the LaBr<sub>3</sub>(Ce) detector. Data acquired on November 25.

<b>nmr (10 kGauss)</b>	<b>Gaussmeter (kGaus)</b>	<b>net counts</b>	<b>Yield</b>
0.209941	2.090	3150 $\pm$ 70	0.00059 $\pm$ 0.00001
0.210096	2.091	1120 $\pm$ 40	0.00058 $\pm$ 0.00002
0.210405	2.094	900 $\pm$ 40	0.00055 $\pm$ 0.00002
0.210701	2.097	960 $\pm$ 40	0.00059 $\pm$ 0.00002
0.210796	2.190	700 $\pm$ 40	0.00055 $\pm$ 0.00002
0.210998	2.100	810 $\pm$ 40	0.00085 $\pm$ 0.00004
0.211104	2.102	1210 $\pm$ 50	0.00086 $\pm$ 0.00003
0.211309	2.103	1040 $\pm$ 40	0.00086 $\pm$ 0.00003
0.211547	2.106	1160 $\pm$ 40	0.00092 $\pm$ 0.00003
0.211900	2.109	1090 $\pm$ 40	0.00078 $\pm$ 0.00003
0.212106	2.111	1430 $\pm$ 50	0.00130 $\pm$ 0.00004
0.212301	2.113	1870 $\pm$ 50	0.00167 $\pm$ 0.00005
0.212511	2.115	2160 $\pm$ 50	0.00165 $\pm$ 0.00004
0.213104	2.121	1860 $\pm$ 50	0.00168 $\pm$ 0.00005
0.213699	2.127	1480 $\pm$ 50	0.00177 $\pm$ 0.00006

Table 33 Number of net counts of the full energy peak at 843 keV as a function of the nmr and calculated Yield using the Germanium detector. Data acquired on November 24.

nmr (10 kGauss)	Gaussmeter (kGaus)	net counts	Yield	
0.210403	2.094	1720 ±60	0.000 59	±0.00002
0.210704	2.097	520 ±30	0.000 57	±0.00003
0.210752	2.090	1430 ±50	0.000 78	±0.00003
0.210792	2.098	1230 ±50	0.000 91	±0.00003
0.210798	2.098	1210 ±40	0.000 91	±0.00003
0.210896	2.099	1220 ±50	0.000 95	±0.00004
0.211708	2.107	1370 ±50	0.000 99	±0.00003
0.211895	2.109	1600 ±50	0.000 96	±0.00003
0.212012	2.110	1950 ±50	0.001 59	±0.00004
0.212107	2.111	1480 ±50	0.001 61	±0.00005
0.212212	2.112	2030 ±50	0.001 75	±0.00005

Table 34 Number of net counts of the full energy peak at 843 keV as a function of the nmr and calculated Yield using the germanium detector. Data acquired on November 25.

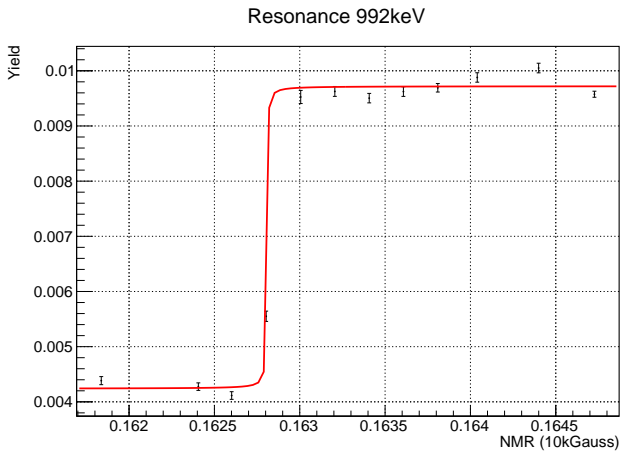
#### F. Fitting of data with an arctangent function

Here we fit the values of Yield obtained in Subsection III.5.D and III.5.E as a function of the nmr probe values. We used an arctangent function for the single resonance at 992 keV and double arctangent function in the case of the two resonances at 1664 and 1684 keV.

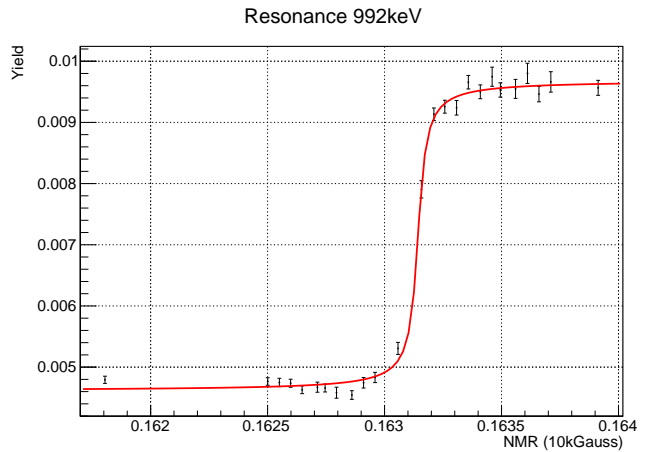
$$f(x) = a \cdot \text{atan}(b(x + c)) + d$$

$$f(x) = a \cdot \text{atan}(b(x + c)) + d + \text{atan}(f(x + g))$$

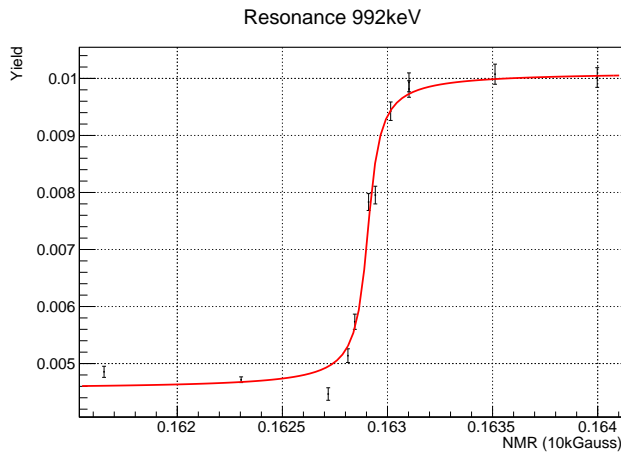
Figure 38, 39 and 40 show the fit obtained for the three resonances.



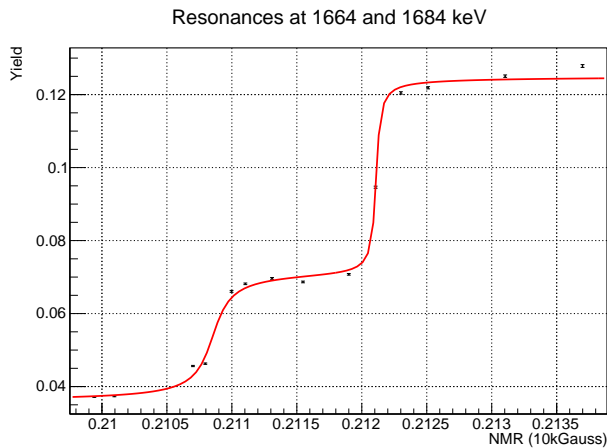
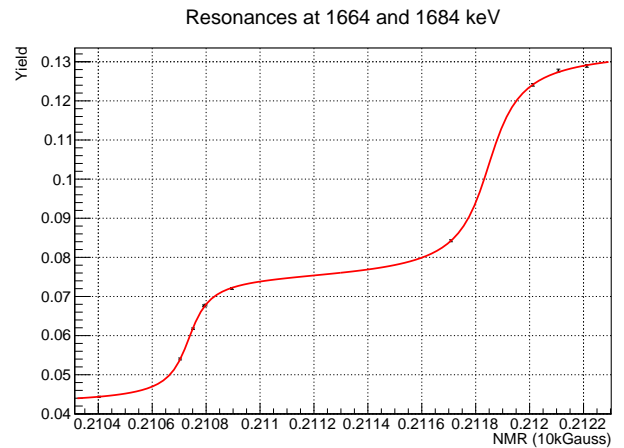
(a) Yield vs nmr for the 992 resonance (day 23/11/22).



(b) Yield vs nmr for the 992 resonance (day 24/11/22).



(c) Yield vs nmr for the 992 resonance (day 25/11/22).

Figure 38 Yield vs nmr for the 992 keV resonance. Data acquired using the LaBr<sub>3</sub>(Ce) detector.(a) Yield vs nmr for the 1664 and 1684 keV resonances, LaBr<sub>3</sub>(Ce) detector (day 24/11/22).(b) Yield vs nmr for the 1664 and 1684 keV resonances, LaBr<sub>3</sub>(Ce) detector (day 25/11/22).Figure 39 Yield vs nmr for the 1664 keV and 1684 keV resonances. Data acquired using the LaBr<sub>3</sub>(Ce) detector.

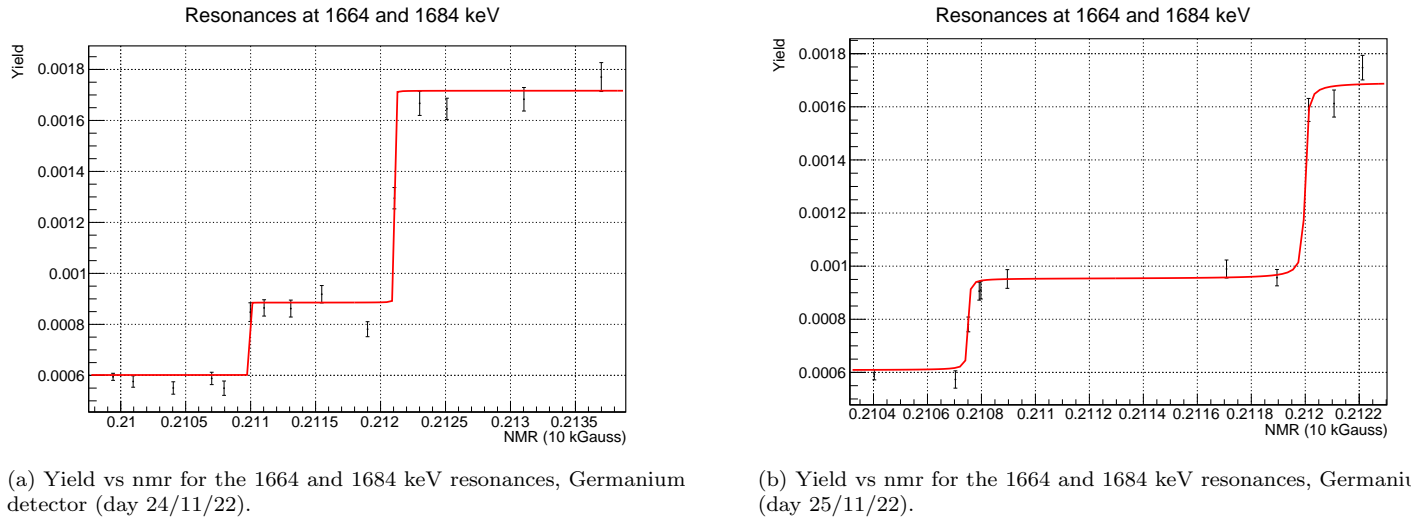


Figure 40 Yield vs nmr for the 1664 keV and 1684 keV resonances. Data acquired using the Germanium detector.

In Tab. 35, 36 and 37 are reported the values of the inflex of the arctangent (or double arctangent) function labelled as  $c$  and  $g$  respectively. We also calculated the resonance widths ( $\Gamma_c$  and  $\Gamma_g$  respectively). The resonance width is obtained from the parameter  $b$  (and  $f$  in the case of the double arctangent function) as  $\Gamma = \frac{2}{b}$ .

	$c$ [10 kGauss]	$\Gamma$ [10 kGauss]
<i>LaBr<sub>3</sub>(Ce)</i> 23/11	-0.162 807 ± 0.000003	0.000 006 ± 0.000003
<i>LaBr<sub>3</sub>(Ce)</i> 24/11	-0.163 143 ± 0.000004	0.000 054 ± 0.000004
<i>LaBr<sub>3</sub>(Ce)</i> 25/11	-0.162 907 ± 0.000004	0.000 087 ± 0.000004

Table 35 Fit parameters of the resonance at 992 keV for LaBr<sub>3</sub>(Ce) detector.

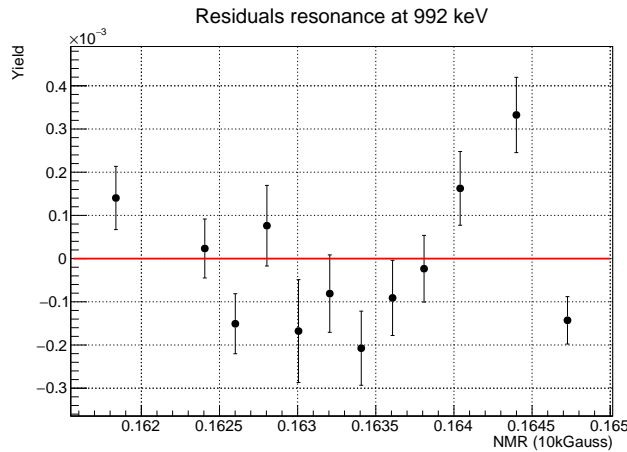
	$c$ [10 kGauss]	$\Gamma_c$ [10 kGauss]
<i>Germanium</i> 24/11/22	-0.210 997 ± 0.000002	0.000 000 2 ± 0.0000004
<i>Germanium</i> 25/11/22	-0.210 751 ± 0.000003	0.000 01 ± 0.00001
<i>LaBr<sub>3</sub>(Ce)</i> 24/11	-0.210 853 ± 0.000003	0.000 213 ± 0.000004
<i>LaBr<sub>3</sub>(Ce)</i> 25/11	-0.210 736 ± 0.000001	0.000 116 ± 0.000003

Table 36 Fit parameters of the resonance at 1664 keV for LaBr<sub>3</sub>(Ce) and Germanium detector.

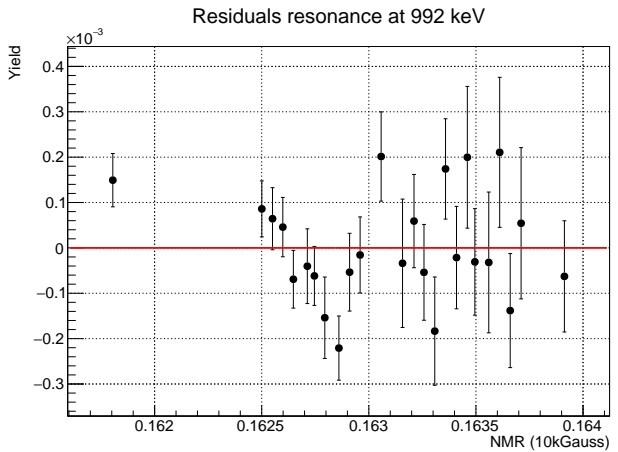
	$g$ [10 kGauss]	$\Gamma_g$ [10 kGauss]
<i>Germanium</i> 24/11/22	-0.212 106 00 ± 0.00000006	0.000 000 9 ± 0.0000005
<i>Germanium</i> 25/11/22	-0.211 999 ± 0.000006	0.000 013 ± 0.000003
<i>LaBr<sub>3</sub>(Ce)</i> 24/11	-0.212 110 0 ± 0.0000007	0.000 049 ± 0.000004
<i>LaBr<sub>3</sub>(Ce)</i> 25/11	-0.211 848 ± 0.000007	0.000 177 ± 0.000005

Table 37 Fit parameters of the resonance at 1684 keV for LaBr<sub>3</sub>(Ce) and Germanium detector.

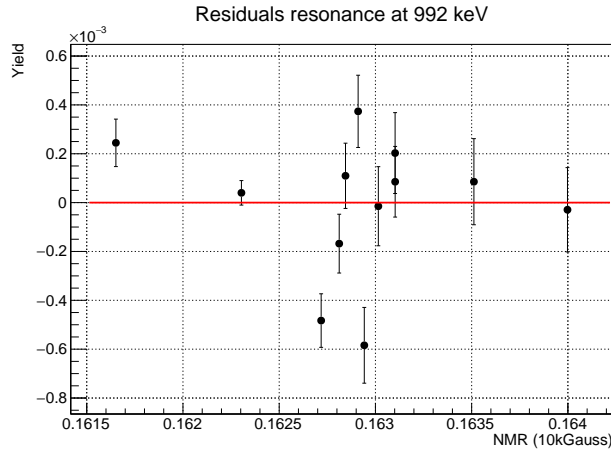
In Fig. 41 are reported the residuals of the fit of the data for the 992 keV resonance with an arctangent function. We also reported the residuals for the fit of the data relative to the 1664 and 1684 keV resonances using LaBr<sub>3</sub>(Ce) detectors in Fig. 42 and with Germanium detector in Fig. 43. The errors are the ones on the y values. The residuals are acceptable ( $|y_{exp} - y_{th}| < 3\sigma$ ) for the 992 keV resonance and also for the 1664 and 1684 resonances with the exception of the data acquired on 24/11 with the LaBr detector (Fig. 42a).



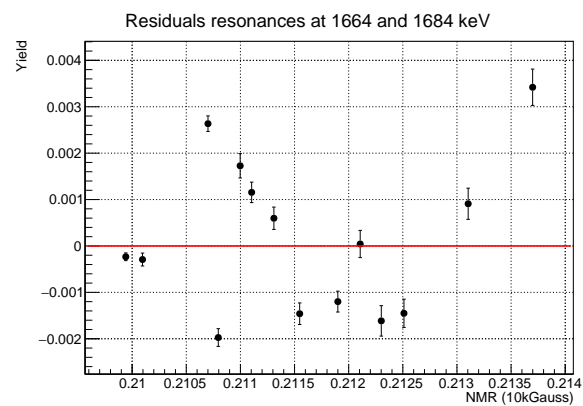
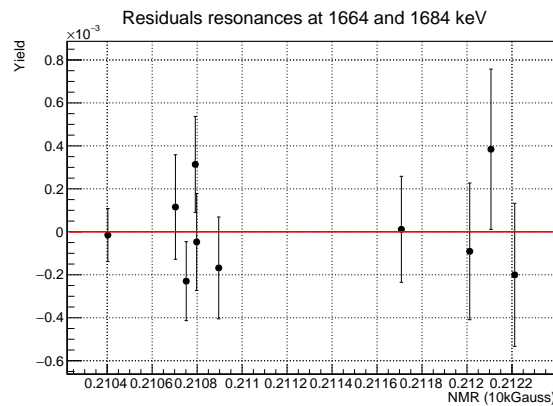
(a) Residuals for the 992 resonance (day 23/11/22).

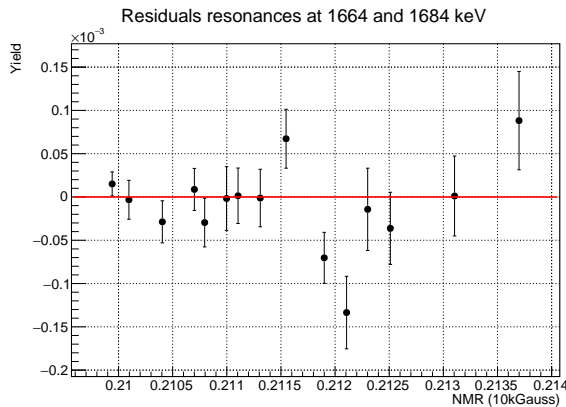


(b) Residuals for the 992 resonance (day 24/11/22).

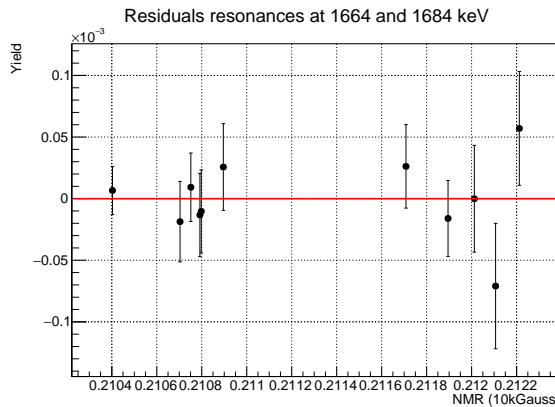


(c) Residuals for the 992 resonance (day 25/11/22).

Figure 41 Residuals for the 992 keV resonance. Data acquired using the LaBr<sub>3</sub>(Ce) detector.(a) Residuals for the 1664 and 1684 keV resonances, LaBr<sub>3</sub>(Ce) detector (day 24/11/22).(b) Residuals for the 1664 and 1684 keV resonances, LaBr<sub>3</sub>(Ce) detector (day 25/11/22).Figure 42 Residuals for the 1664 keV and 1684 keV resonances. Data acquired using the LaBr<sub>3</sub>(Ce) detector.



(a) Residuals for the 1664 and 1684 keV resonances, Germanium detector (day 24/11/22).



(b) Residuals for the 1664 and 1684 keV resonances, Germanium detector (day 25/11/22).

Figure 43 Residuals for the 1664 keV and 1684 keV resonances. Data acquired using the Germanium detector.

In Table 38 and 39 we report the values of the energies tabulated in the LNL tables corresponding to the nmr values corresponding to the inflection points of the arctangent ( $|c|$  and  $|g|$ ) and the shift in keV of these energy values compared with the reference ones (i.e. the ones of the resonances). In this way we are able to estimate how much the energies obtained from previous calibrations of the accelerator are far from the real ones.

From the values obtained for the shifts it is possible to see that they change on different days. For this reason, even if the set up was the same, we decided to keep data sets acquired on different days separated. Considering the shifts for the same day we also observe that the shift for the resonances at higher energies is larger respect to the shift for the 992 keV resonance. This may imply an energy dependence of the shift. Finally, the values obtained for the shifts of the 1664 and 1684 keV using the LaBr<sub>3</sub>(Ce) and the Germanium detectors are similar, but not the same in all the case. This may be due the low statistic we had with the Germanium detector, since it was not placed close to the scattering point.

	$E_{tab,992}$ [keV]	shift [keV]
<i>LaBr<sub>3</sub>(Ce)</i> 23/11	1004.76	$12.90 \pm 0.03$
<i>LaBr<sub>3</sub>(Ce)</i> 24/11	1008.90	$17.04 \pm 0.03$
<i>LaBr<sub>3</sub>(Ce)</i> 25/11	1005.99	$14.13 \pm 0.03$

Table 38 Shift with respect to the energy of the resonance at 991.86 keV for LaBr<sub>3</sub>(Ce) detector.

	$E_{tab,1664}$ [keV]	shift [keV]	$E_{tab,1684}$ [keV]	shift [keV]
<i>Germanium</i> 24/11/22	1687	$22.6 \pm 0.2$	1705	$21.43 \pm 0.13$
<i>Germanium</i> 25/11/22	1683	$18.6 \pm 0.2$	1703	$19.43 \pm 0.13$
<i>LaBr<sub>3</sub>(Ce)</i> 24/11	1685	$20.6 \pm 0.2$	1705	$21.43 \pm 0.13$
<i>LaBr<sub>3</sub>(Ce)</i> 25/11	1683	$18.6 \pm 0.2$	1701	$17.43 \pm 0.13$

Table 39 Shift with respect to the energy of the resonances at 1664.4 and 1683.57 keV for LaBr<sub>3</sub>(Ce) and Germanium detector.

In addition, we used the parameter  $\Gamma$  obtained for the resonance at 992 keV measured on November 25 to calculate the width of the resonance in keV. We chose to consider this data acquisition since in the region of interest for the resonance there are more experimental points. As we did for the energy shift, we used the tables provided by the laboratory to derive a correspondence between the nmr values and the energy. We eventually get  $\Gamma = 1.07 \pm 0.05$  keV, where the error is obtained through propagation considering only the contribution from  $\Gamma$  in Table 35. It is to be noted that the contributions to this width does not come entirely from the resonance width, but the major contribution arises from the energy width of the accelerator. Since the resonance width is very small,  $\Gamma$  can be considered a measurement of the energy width of the accelerator.

#### IV. CONCLUSIONS

We collect here some conclusions deduced from the previous analysis

- Comparing the two LaBr<sub>3</sub>(Ce) detectors we observed that ch0 has a better energy resolution than ch1 one. As a consequence, the signal to noise ratio and the efficiencies are higher for ch0. For the CeBr<sub>3</sub> detector, instead, the efficiency behaviour of ch0 is the same as ch1.
- In the width calibration we extracted a rough trend for the FWHM behaviour as a function of the energy. As already pointed out, the gap between the 511 keV gamma peak and the other three full energy peaks is large. To extract a more precise behaviour of the FWHM we may have taken more energy peaks in the energy region which was not covered.
- We calculated the efficiencies using different methods. For the <sup>60</sup>Co source the efficiencies obtained with the coincidences are compatible with the ones obtained with the full energy peak method. On the other hand, the efficiencies we obtained for the 511 keV peak are different for the two methods. A possible explanation may be the fact that in the two methods the background events are removed differently and the coincidence method may be more effective in removing the background.
- The number of the net counts of the full energy peaks depends on several contributions: we took into account for the background subtraction, however we did not consider the summing out effects. This probably explains the irregular trend of the efficiency behaviour as a function of the energy (in particular it does not decrease with the energy).
- We tested the timing response for the CeBr<sub>3</sub> detectors through a measurement of the speed of light. Usually, inorganic crystals are not suitable for precise timing measurements, however in our case the measurement is accurate and we can conclude that the CeBr<sub>3</sub> have a very good timing response.
- The calibration of the AN2000 accelerator was more complicated than expected. We faced several problems, first of all the difference in the energy shifts on different days. For this reason we decided to keep the data acquired on different day separated and we cannot give a unique value for the shift in energy at a specific energy. The shift between the values tabulated is probably energy dependent, since we got different shifts for the resonance at 992 keV and the two resonances at higher energies. Eventually, the energy width of the accelerator may be a contribution to the differences in the shift values.

#### REFERENCES

- [1] Gilmore G. R., *Practical Gamma-ray Spectrometry*, John Wiley & Sons, 2008
- [2] Knoll G. F., *Radiation Detection and Measurement*, John Wiley & Sons, Inc., 2010
- [3] CAEN, User Manual UM5960 CoMPASS, Rev. 18 - February 15 th , 2022
- [4] CAEN Digital Pulse Height Analyser - a digital approach to Radiation Spectroscopy, Application Note AN2508, September 2011
- [5] CAEN, User Manual WP2081 Digital Pulse Processing in Nuclear Physics, Rev. 4 - June 12 th , 2017
- [6] Caciolli A., *Misure di sezioni d'urto di diffusione elastica ed emissione di protoni su nuclei leggeri a energie comprese tra 3 e 7 MeV (Tesi di laurea)*, Università degli Studi di Firenze, 2005
- [7] Iliadis C., *Nuclear Physics of Stars*, Wiley-VCH, 2015